

CHARACTERIZATION OF CALCIFICATIONS IN DISEASED HUMAN AORTIC VALVES: A
RAMAN STUDY

A Thesis

Presented to the Faculty of the Graduate School
of Cornell University

In Partial Fulfillment of the Requirements for the Degree of
Master of Science

by

Siyuan (Derek) Hu

August 2021

© 2021 Siyuan Hu

ABSTRACT

The formation of biogenic minerals in human aortic valves is an increasingly prevalent cardiovascular pathology lacking effective treatment options except valve replacement surgery. Much research has focused on cell signaling pathways and maladaptive remodeling of the valvular matrix. Little is known, however, about the pathological mineralization process from a materials science perspective, potentially due to a lack of appropriate characterization tools. In this thesis, excised human patient valves with varying degrees of calcification were scanned via micro-CT, processed, and analyzed via Raman microscopy in series with histological staining. Raman microscopy enabled characterization of mineral and organic matrix composition in the context of pathology. Carbonated hydroxyapatite was found to be the predominant phase of valvular calcification, though traces of whitlockite and octacalcium phosphate were also detected. We found that the mineral crystallinity of valvular calcification was higher for female than male patients. Though calcifications were extremely heterogeneous across and among patients in terms of size, mineralization density, matrix composition, etc., small calcifications tended to associate strongly with lipids, while large calcifications with collagen. The association of specific matrix species with calcifications size could reflect different events in the pathological progression of the disease (e.g., inflammation and fibrosis), and warranted further investigation. This thesis laid the groundwork for incorporating Raman microscopy into future studies of pathogenesis of calcific aortic valve disease.

BIOGRAPHICAL SKETCH

Derek is a nonconformist. Where materials science collides with biomedical science (e.g., translational medicine, healthcare) invigorates his passion on solving the next problem. Derek believes that true science is of beauty and aims to integrate art and philosophy into technology and product design. As an advocate of Kantian ethics, Derek embraces the duty of creative innovation for the better of humanity.

ACKNOWLEDGEMENTS

The recognition and support I got from the people in Cornell were the best antidote to the covid crisis. First, I would like to thank my advisor Dr. Lara Estroff for her guidance during my stay at Cornell. The degree of freedom that she granted me to explore science has changed the way I think and approach challenges. I would like to thank Dr. Jonathan Butcher and Dr. Eve Donnelley for coming up with the project and the continuous support along the way.

I would like to thank all the people that have taught me science and helped me with my experiments. Thank you to Erik Taylor, Ablajan Mahmut, Terence Gee, Teresa Porri (BRC), Jackie Fretz (Yale), John Grazul, Phillip Carubia, and Marco Hiller. I would like to thank the Estroff group for creating a welcome and supporting atmosphere.

Last but foremost, I would like to thank my predecessor, my mentor, and my friend Jennie Kunitake. Jennie has spent a tremendous amount of time on me, and her work has always been a source of motivation. It is truly a privilege to have Jennie as my mentor. This work was funded by grants from the National Institutes of Health.

TABLE OF CONTENTS

Biographical Sketch.....	iii
Acknowledgements	iv
Table of Contents.....	v
List of Figures.....	vii
List of Tables	x
CHAPTER 1 INTRODUCTION and BACKGROUND.....	1
1.1 Biomineralization.....	1
1.2 The Aortic Valve and the Valve Disease.....	2
1.2.1 Human Aortic Valve	2
1.2.2 Calcific Aortic Valve Disease	3
1.2.3 Etiology of CAVD	4
1.3 Characterization of Valvular Calcifications	9
1.3.1 Characterization Techniques	9
1.3.2 Raman Signatures of Pathological Mineralization	11
1.4 Summary and Outlook.....	18
CHAPTER 2 MAPPING AND PROFILING THE HETEROGENEITY OF CALCIFICATIONS IN DISEASED HUMAN AORTIC VALVES.....	28
2.1 Introduction	28
2.2 Materials and Methods.....	30
2.2.1 Human aortic valve samples	30
2.2.2 Micro-CT scanning, model generations, and index sum scoring.....	30
2.2.3 Sample preparation and histology.....	31
2.2.4 Raman data collection	32
2.2.5 Raman combinational maps	33
2.2.6 Mean Raman spectra and statistical analysis	34
2.3 Results.....	35
2.3.1 Micro-CT analysis.....	36
2.3.2 Raman mapping of valvular calcifications.....	39
2.3.3 Analysis of mean Raman spectra and hierarchical clustering.....	48
2.4 Discussion	54
CHAPTER 3 CONCLUSION & FUTURE DIRECTIONS.....	59

APPENDIX.....	63
A.1 Graphs of Calcified Valve Samples.....	63
A.2 Aortic Valve Sample Sections	64
A.3 Carbonate Content vs. Crystallinity	66
A.4 Heterogeneity.....	67
A.5 Raman Peak Assignments.....	68

LIST OF FIGURES

<p>Figure 1. 1. The trilaminar structure of the aortic valve. The endothelial cells (ECs) forge a tight lining on the valve surface, while the interstitial cells (VICs) spread among the three layers, fibrosa on the aortic side, spongiosa on the middle, and ventricularis on the ventricular side (Reprinted from Ref. 9, with permission from Elsevier).....</p> <p>Figure 1. 2. The biochemical pathways thought to be involved in the progression of CAVD. Endothelial dysfunction is believed to be the onset that allows lipid infiltration. Immune cells are then recruited from the bloodstream to combat these “foreign enemies”, secreting chemokines and cytokines that trigger chronic inflammation. The following fibrocalcific remodeling of the ECM accelerates osteochondral differentiation of valvular cells, associated with the activation of renin-angiotensin system and angiogenesis. Mineralization, via either dystrophic calcification or heterotopic ossification, becomes the endpoint of CAVD (Reprinted from Ref. 9, with permission from Elsevier).....</p> <p>Figure 1. 3. The arrangements of minerals and collagen in both physiological and pathological mineralization. a, b). SEM images of mineralized collagen fibrils in human fetal bone. c-n). Both H&E-stained graphs and SEM images are shown for three representative breast cancer calcifications. c-f). Fibroadenoma. G-f). Sclerosing adenosis. k-n). Low-grade micropapillary pattern DCIS (Reprinted from Ref. 4, with permission from Wiley).....</p> <p>Figure 1. 4. Raman spectra of three representative lipid species. A). Saturated fatty acids like palmitic acid have a characteristic peak complex at region III. B). Triacylglycerols have a characteristic peak at 1740 cm^{-1}, assigned to the ester bond. C). Cholesterol esters can be discerned from peaks at 429 cm^{-1} and 702 cm^{-1}, assigned to the backbone vibrational mode (Reprinted from Ref. 71, with permission from Wiley).....</p>	<p>3</p> <p>5</p> <p>15</p> <p>17</p>
<p>Figure 2. 1. Micro-CT modeling of a patient valve sample and index sum scoring. A). A macroscopic graph of a representative calcified human aortic valve sample. B). A micro-CT model of the same valve sample. Color gradient (yellow to red) and transparency are coupled to depict regions of calcifications. C-G). Voxels were assigned to five bins: tissue (purple, C), light calcification (red, D), medium calcification (green, E), heavy calcification (yellow, F), and extremely heavy calcification (pink, G). H). The micro-CT scores of all 21 samples. The wide range of the scores demonstrated the range of mineralization density in aortic valves at the time of surgery.</p> <p>Figure 2. 2. Univariate Raman maps and mean Raman spectra show that minerals associate with lipids in small calcifications. A, E, I). Light optical microscope images of three small calcifications. B-D, F-H, J-L). Univariate Raman maps of the three calcifications. Peak areas filters of $\nu_1\text{ PO}_4^{3-}$, CH_2 twisting, and C-O-C stretching were used for constructing univariate Raman maps of mineral, lipid, and PMMA, accordingly. M). Six mean Raman spectra from six small calcifications with size ranging from $83\text{-}473\text{ }\mu\text{m}^2$ show strong association between CHA and lipid. Two characteristic spectral regions of lipids are colored in yellow.</p> <p>Figure 2. 3. An uncommon yet fascinating small calcification associated with lipid. A). Light optical image of the calcification of interest. B, C). Histological staining of the same calcification. von Kossa (B) showed the presence of the calcium phosphate and Movat Pentachrome (C) identified collagen as a major species of the surrounding matrix. D-G). Raman combinational maps showing CHA (magenta) and lipid (yellow) juxtaposed on collagen fibers (clover). H) The three bases Raman spectra for CHA, collagen, and lipid.</p> <p>Figure 2. 4. Univariate Raman maps and mean Raman spectra show that minerals associate with collagen in large calcifications. A, E, I). Light optical microscope images of the periphery of three large calcifications. B-D, F-H, J-L). Univariate Raman maps of the three calcifications. Peak areas filters of $\nu_1\text{ PO}_4^{3-}$, Amide III, and C-O-C stretching were used for constructing univariate Raman maps of mineral, collagen, and PMMA, accordingly. M). Five mean Raman spectra from five medium to large</p>	<p>38</p> <p>41</p> <p>42</p>

calcifications with size ranging from 1679-22766 μm^2 show strong association between CHA and collagen. Two characteristic spectral regions of collagen are colored in green..... 44

Figure 2. 5. A large calcification bounded by collagen fibers. A). Light optical image of the calcification of interest. B, C). Histological staining of the same calcification: von Kossa (B) showed the presence of the calcium phosphate and Movat Pentachrome (C) identified the surrounding matrix as highly dense yet poorly organized collagen fibers. D-G). Raman combinational maps showing CHA (magenta) situated among collagen fibers (clover). H) The two bases Raman spectra for CHA and collagen..... 45

Figure 2. 6. Raman univariant mapping reveals the correlation between calcification size and matrix species. Small calcifications ($n = 34$), with size less than 500 μm^2 , are intimately associated with lipids, and less with collagen. On the contrary, large calcifications ($n = 28$), with size large than 2000 μm^2 , are more associated with collagen fibers, and less with lipids. Medium calcifications ($n = 41$), with size ranged from 500 to 2000 μm^2 , show combined traits of the other two groups. 46

Figure 2. 7. A rarely found whitlockite cluster surrounded by collagen fibers and lipid species. a). Light optical image of the calcification cluster. b, c). Histological staining of the same calcification cluster: von Kossa shows negligible signals of calcification (b) and Movat Pentachrome (c). d-g). Raman combinational map showing whitlockite (magenta), collagen fibers (clover), and cholesterol (yellow). h) The three bases Raman spectra for CHA, collagen, and cholesterol..... 47

Figure 2. 8. The mean spectrum of 90 mean Raman spectra. A mean spectrum of 90 averaged mean Raman spectra was plotted on top of the standard deviation to reflect the variations of mineral-matrix species present among the 90 calcifications of interest..... 49

Figure 2. 9. Examples of single vs. aggregate calcifications and the correlation between mineral form and calcification size. A, B). light optical microscope images of representative small (A) and aggregate (B) calcifications with similar calcification size. C). A box plot shows that the mean size of aggregate calcifications ($n = 41$) is much larger than that of single calcifications ($n = 43$). The color of dots is consistent with the 5 hierarchical clusters. 50

Figure 2. 10. Hierarchical clustering of calcifications using 5 mineral-matrix metrics from Raman. The rows represent the fingerprints of calcifications ($n = 84$ from 8 patients), while the columns correspond to metrics (5 mineral-matrix metrics, with gender and mineral form). Micro-CT scores are shown on the left and colored based on the 5 clusters. 53

Figure 2. 11. Lipid vs. collagen content and crystallinity vs. gender. A). Linear regression is used to fit a scatter plot of lipid to protein ratio vs. collagen to matrix ratio. Though the data has high variation ($R^2 = 0.357$), an inverse relationship between the two parameters is clear ($p < 0.001$). B). A box plot of crystallinity vs. gender shows that the mean crystallinity of calcifications from female patients is higher than that of male patients ($p < 0.003$). The color of dots is consistent with the 5 hierarchical clusters. 53

Figure A. 1. Macroscopic graphs and micro-CT models of all 21 calcified aortic valve samples. A-U). 21 pairs of macroscopic graphs (left) and micro-CT models (right), along with the sample ID and the micro-CT scores (in bracket). The sample ID and micro-CT scores correspond to the ones in Figure 2.1.H. 63

Figure A. 2. Movat Pentachrome stain of a valve section from a female patient with a micro-CT score of 21. Two regions, calcification nodule and whitlockite cluster, are circled. Both aortic and ventricular side of the valve leaflet are labeled. The region of whitlockite cluster is mapped via Raman (Figure 2.7). 64

Figure A. 3. Three serial sections from a patient with a micro-CT score of 434. A). Movat Pentachrome stain is used to study the tissue architecture. B). von Kossa stain is employed as a guide to determine the regions of interest. C). Raman mapping is performed to explore the mineral-matrix relationships. 65

Figure A. 4. Two scatter plots of mineral crystallinity vs. carbonate content. A). Raw data collected from $\nu_1 \text{PO}_4^{3-}$ and $\nu_1 \text{CO}_3^{2-}$ are used without any data processing. The Low R^2 and high p -value shows that the two parameters have no relationship. B). Processed data with manual PMMA subtraction and peak fitting (Lorentzian) on $\nu_1 \text{PO}_4^{3-}$ shows a positive relationship between mineral crystallinity (inverse

of FWHM) and carbonate content. However, since we cannot fully grasp the rationale behind data processing, plot A is chosen for the final configuration. 66

Figure A. 5. Heterogeneity of valvular calcifications across patients. Two types of patients are summarized. Type A patients (cyan, $N = 3$) have calcifications distributed across 4 out of 5 clusters, while Type B patients (magenta, $N = 4$) have most calcifications concentrated within one cluster. 67

LIST OF TABLES

Table 1. 1. Primary Raman bands assignments on bone. The table explains the vibrational modes that attribute to the major Raman peaks for both mineral and matrix species in the spectral range of 400-1700 cm^{-1} (Reprinted from Ref. 55, with permission from Elsevier).....	14
Table A. 1. The distribution of 84 calcifications in 5 clusters with respect to patients. Patients with micro-CT scores of 91, 310, and 516 have calcifications dispersed in multiple clusters (type A), while patient with scores of 158, 225, 263, and 434 have calcifications concentrated within a cluster (type B)	67
Table A. 2. Raman band assignments. The spectral range of Raman peaks used in this study to calculate peak areas (and peak width).	68

CHAPTER 1

INTRODUCTION AND BACKGROUND

1.1 Biomineralization

Biomineralization is a multi-disciplinary field comprising the study of minerals formed by organisms. Since organisms across all five kingdoms are both capable of producing minerals and active players constantly shaping the living environment, it is not surprising that biogenic minerals play an indispensable role among multiple disciplines, such as oceanography, archeology, and dentistry¹. One representative example of biogenic minerals is hydroxyapatite (HA, $\text{Ca}_{10}(\text{PO}_4)_6(\text{OH})_2$). The stoichiometric form is rarely found in nature. Instead, multiple ionic substitutions have been recorded including Na^+ , K^+ , Mg^{2+} , Sr^{2+} , CO_3^{2-} , Cl^- , F^- ². Besides ionic substitutions, the process of biomineralization is further complicated by the subtle interactions between inorganic minerals and organic molecules.

Biomineralization in the human body can be divided into two categories. One is physiological mineralization, such as bones and teeth, where the minerals produced by cells are dispersed into an extracellular matrix (ECM), often resulting in an exquisite, hierarchical structure to maximize desired functionalities. The deposition and growth sites of these minerals, according to a recently proposed “stenciling principle”, are likely pre-determined by genetics and regulated by multiple layers of control³. The other is pathological mineralization, often associated with abnormalities in both the cells (e.g., cell death or cell trans-differentiation) and the ECM (e.g., fibrosis), led by metabolic disorders or diseases⁴. Examples of pathological mineralization include breast microcalcifications⁵, kidney stones⁶, and calcified heart valves⁷. While both categories of calcifications will serve as references to

establish the context, this thesis focuses on the pathological minerals found in human aortic valves.

1.2 The Aortic Valve and the Valve Disease

1.2.1 Human Aortic Valve

The human heart has four valves, the major function of which is to facilitate unidirectional blood flow and to prevent regurgitation⁷. The aortic valve, located at the aortic root that connects the left ventricle and the aorta, is no exception: it opens during systole, allowing blood outflow, and closes during diastole, preventing blood backflow. It is estimated that the number of systole-diastole cycles reaches 40 million within a year and 3 billion over a lifetime of 75 years⁸. Behind such superior performance is a unique structure: the ECM of each leaflet, or cusp, of the aortic valve has three distinct layers (Fig. 1.1)⁹. Fibrosa, located on the aortic side, contains largely circumferentially oriented collagen fibers (type I and III) to provide the overall structural stiffness. Spongiosa, the middle layer, is characterized by abundant proteoglycans and glycosaminoglycans (GAGs) to adhere and lubricate the two outer layers¹⁰. Ventricularis, positioned on the ventricular side, is mainly composed of radially oriented elastin fibers to absorb and dissipate shear stress. There are two dominant cell types in the aortic valve. The valvular endothelial cells (VECs) tightly line the valvular surface and actively respond to external stimuli, while the valvular interstitial cells (VICs) reside within the trilaminar ECM. In adults, most VICs are highly plastic but exhibit a quiescent phenotype that resembles fibroblasts under homeostasis⁹.

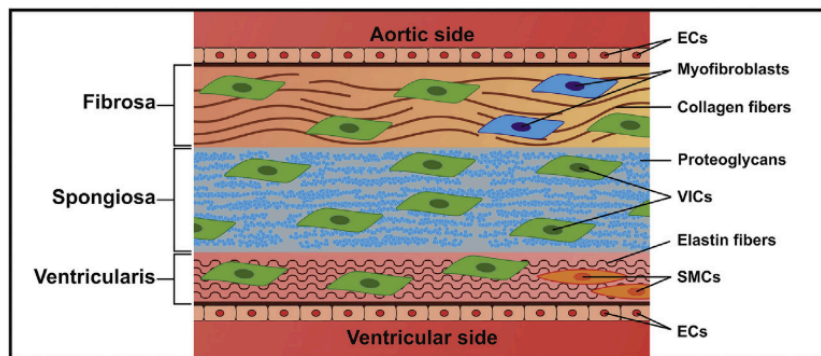


Figure 1. 1. The trilaminar structure of the aortic valve. The endothelial cells (ECs) forge a tight lining on the valve surface, while the interstitial cells (VICs) spread among the three layers, fibrosa on the aortic side, spongiosa on the middle, and ventricularis on the ventricular side (Reprinted from Ref. 9, with permission from Elsevier).

1.2.2 Calcific Aortic Valve Disease

Calcific aortic valve disease (CAVD) is a complex, multifaceted disease involving thickening and stiffening of the aortic valve and resulting in chronic heart failure⁹. There is a strong imperative to understand the biomineralization pathways that lead to CAVD, due to the poor survival after disease symptoms appear. There are two clinical stages of the pathology: aortic sclerosis (valve thickening with some calcification that does not hinder normal valvular functions) and aortic stenosis (heavily remodeled and calcified valves that obstruct blood flow). While the maladaptive remodeling of the aortic valve induces both pressure overload and left ventricular hypertrophy, the progression of CAVD can span across one to two decades without noticeable clinical signs, especially in men, followed by lethal symptoms including heart failure, angina, and syncope^{11,12}. Besides congenital leaflet abnormalities, e.g., bicuspid aortic valve, major clinical risk factors include advanced age, male sex, smoking, hypertension, metabolic syndrome, diabetes/hyperglycemia, and kidney disease^{7,12}.

According to the *AGES-Reykjavík* study (2014), 4.3% of the individuals over 70 years of age have severe aortic stenosis and it is predicted that such a rate will increase 2.4-fold by 2040 and triple by 2060, potentially due to the aging of baby boomers and a lack of prognostic tools^{12,13}. Doppler Echocardiography (an imaging system via the use of high frequency sound waves) is the primary diagnostic modality to date. The crude reality is that there is no pharmaceutical treatment available for reversing or even relieving the symptoms of CAVD, and valve replacement, performed surgically or via a transcatheter, at late-stage CAVD is currently the only effective treatment option⁸. Compared to surgical aortic valve replacement, transcatheter aortic valve replacement tends to have a reduced surgical complication, longer life expectancy, and lower projected lifetime cost^{14,15}. The development of diagnostic and prognostic tools can open a therapeutic window for CAVD prior to the seemingly irreversible late-stage calcification⁸.

1.2.3 Etiology of CAVD

Contrary to a merely age-related dystrophic calcification (calcification occurring in degenerated or necrotic tissue), the valvular degeneration of CAVD was first recognized as *“an actively regulated disease process in need of further study”* by a working group assembled by the National Heart, Lung, and Blood Institute (NHLBI) in 2011¹¹. The influence of pro-calcific microenvironment on mineral growth is truly a multidisciplinary study that involves mechanics (e.g., disturbed hemodynamic patterns), biology (e.g., cellular phenotypic change), chemistry (e.g., proteolysis and matrix remodeling), and materials science (e.g., mineral nucleation and growth). Although many details remain elusive, the progression of CAVD can be roughly divided into four stages: endothelial dysfunction, chronic inflammation, fibrosis (aortic sclerosis), and mineralization (aortic stenosis)⁹. Multiple stages can occur at

different sites of the same cusp concomitantly. Details regarding each stage are discussed below (Fig. 1.2).

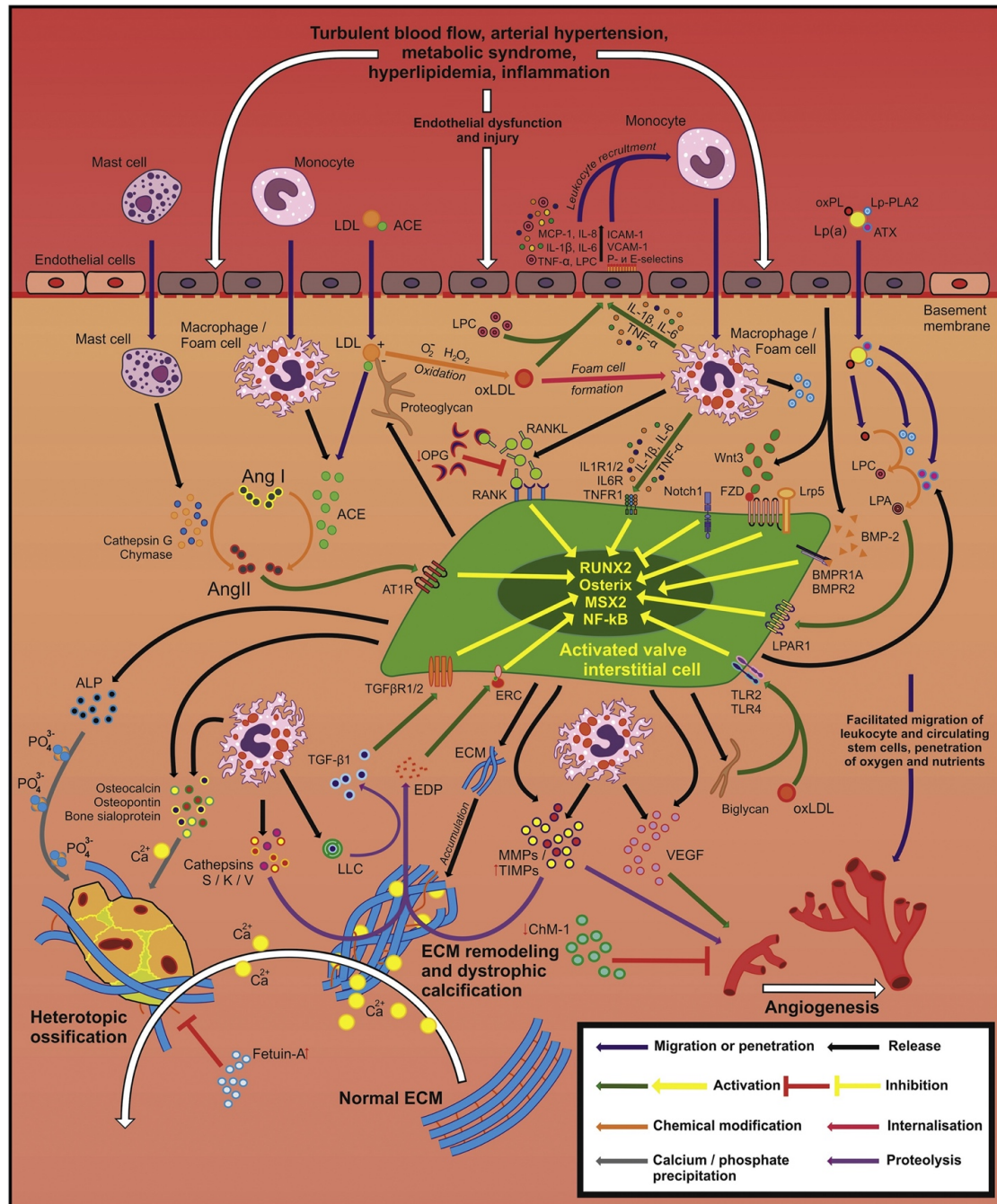


Figure 1. 2. The biochemical pathways thought to be involved in the progression of CAVD. Endothelial dysfunction is believed to be the onset that allows lipid infiltration. Immune cells are then recruited from the bloodstream to combat these “foreign enemies”, secreting chemokines and cytokines that trigger chronic inflammation. The following fibrocalcific remodeling of the ECM accelerates osteochondral differentiation of valvular cells, associated with the activation of renin-

angiotensin system and angiogenesis. Mineralization, via either dystrophic calcification or heterotopic ossification, becomes the endpoint of CAVD (Reprinted from Ref. 9, with permission from Elsevier).

Endothelial dysfunction is commonly believed to be the onset that triggers a cascade of events leading to aortic stenosis^{8,9,16–19}. A change in the hemodynamic pattern (e.g., from pulsatile, laminar flow to oscillatory, turbulent flow), though the cause of which remains largely unknown, can alter the local mechanical state (e.g., shear stress and tensile strain) near the valve surface and injure the endothelial lining^{9,17}. These injured VECs can no longer properly regulate surface coagulation nor limit surface permeability, thus allowing lipid molecules to infiltrate into the organic matrix. Meanwhile, the VECs in the injured regions are activated by upregulating adhesion molecules (e.g., ICMA-1, VCAM-1, and E-selectin) and chemokines (e.g., IL-8, IL-13) to attract circulating monocytes and leukocytes, thus triggering inflammation^{17,19,20}.

Chronic inflammation paves the way for pathological leaflet remodeling^{9,12,20–23}. Infiltrated lipid species (e.g., low-density lipoprotein, or LDL), stabilized by the electrostatic attraction between lipoproteins and proteoglycans, can accumulate, and can then be further oxidized and enzymatically modified into detrimentally bioactive species (e.g., ox-LDL and lysophospholipids)^{12,21}. To engulf these reactive lipid species, immune cells (e.g., monocyte-derived macrophages, T lymphocytes, and mast cells) are recruited, releasing pro-inflammatory cytokines (e.g., IL-6, TNF- α , and TGF- β 1)^{22,23}. Besides self-amplifying the recruitment of immune cells, these cytokines are believed to play active roles in CAVD, such as exacerbating endothelial injury, triggering cell signaling (e.g., NF κ B pathway), and inducing cell phenotypic changes (e.g., EndMT)^{9,12,23}.

Fibrosis, commonly perceived as a default downstream event of human wound healing, is another hallmark of CAVD^{8,9,24–28}. The growth of dense yet poorly organized

collagen bundles in valvular leaflets can be attributed to two conflicting processes: fibrosis and proteolysis. Fibrosis is closely associated with VICs, when the cells undergo a phenotypic change from fibroblasts to myofibroblasts and actively synthesize collagen fibers into the ECM. Influenced by both biochemical (TGF- β 1) and mechanical cues (e.g., increased stiffness²⁴), the phenotypic change of VICs is potentially activated via both TGF- β 1/Smad and Wnt/ β -catenin signaling pathways²⁵. Meanwhile, proteolysis degrades the valvular ECM, when cells secrete proteases (i.e., enzymes that degrade proteins), such as MMPs²⁶, TIMP²⁷, and cathepsins²⁸, that target collagen, cells, and elastin, accordingly⁹. In CAVD, fibrosis outweighs proteolysis, but in fact both fibrosis (collagen deposition) and proteolysis (elastin degradation) promote valve stiffening, a mechanical cue necessary for VIC trans-differentiation²⁴, thus completing a vicious circle. Studies have also shown that both the activation of the renin-angiotensin system (RAS)^{29,30} and angiogenesis^{31,32} (i.e., growth of new blood vessels) contribute to fibrosis and transform the valvular ECM into a pro-calcification environment.

Mineralization seems to be the irreversible endpoint that defines CAVD. The cause of this calcification process has been proposed to stem from two distinctive, non-mutually exclusive mechanisms: dystrophic calcification and heterotopic ossification^{9,12,33–37}.

Dystrophic calcification is considered a passive process, where calcium phosphate precipitates either homogeneously or heterogeneously with the aid of damaged matrix fibers³³, apoptotic bodies³⁴, and/or cholesterol crystals^{35,36}. Meanwhile, heterotopic ossification is thought to be an active process, in which cells (e.g., EndMT and trans-differentiated VICs) adopt an osteoblastic phenotype, activate a number of signaling pathways (e.g., Wnt/ β -catenin, NF κ B, and Notch) that converge on the production of transcription factor Runx2, and facilitate osteogenic remodeling of valvular ECM, leading to

mineralized collagen fibers^{9,36,37}. Regardless of the route of mineralization, while disorganized ECM supplies ample physical space, both decreased levels of calcification inhibitors (e.g., fetuin-A, matrix Gla protein)³⁷ and increased levels of pro-calcific molecules (e.g., elastin degradation products, or matrikines)³⁸ likely provide biochemical cues in favor of mineralization.

In summary, a four-step process has been proposed to delineate the major events of CAVD: endothelial dysfunction as the onset, inflammation the trigger, and fibro-calcific remodeling the downstream result⁹. Traditional drugs for treating atherosclerosis (deposition of plaque on artery walls), like statins, have low efficacy on patients with CAVD, potentially due to its incapability of reducing lipoprotein(a) level²⁰. Although some treatments that target VIC trans-differentiation and matrix remodeling at late-stage CAVD have shown some efficacy, more and more researchers start to shift their focus towards the upstream. One *in vivo* murine study found that inhibiting p65 signaling (p65 is a protein of the NFκB heterodimer, which often remains dormant in cytoplasm but gets activated to initiate transcription if the inhibitory protein IκBα dissociates from the protein complex) via IKKβ deletion can mitigate endothelial inflammation even in a pro-CAVD milieu (i.e., osteogenic medium, high fat diet)³⁹. Since multiple signaling cascades converge downstream at the IKK complex, targeting this IKK complex, i.e., IKKβ silencing, can shut down the canonical NFκB pathway, prevent EndMT, and inhibit osteogenic calcification. Meanwhile, advanced molecular imaging tools have recently been employed (e.g., ¹⁸F-sodium fluoride and ¹⁸F-fluorodeoxyglucose PET)^{40,41} to target the asymptomatic progression of CAVD, buying more time for different treatments or even preventing calcification from the onset^{8,9}.

1.3 Characterization of Valvular Calcifications

1.3.1 Characterization Techniques

Plenty of analytical techniques have been applied to investigate biogenic minerals to date. Among them are three techniques, i.e., x-ray diffraction (XRD)^{42,43}, scanning electron microscopy (SEM, with energy dispersive x-ray spectroscopy, or EDS)⁴³⁻⁴⁶, and vibrational spectroscopy⁴⁷⁻⁵¹, that have frequently been employed to characterize calcifications in human aortic valves. Details regarding each method are discussed below.

Since each crystalline substance has a unique x-ray diffraction pattern, XRD has widely been used to determine mineral phases⁵². *Höhling* (1968) reported the presence of hydroxyapatite (HA, $\text{Ca}_{10}(\text{PO}_4)_6(\text{OH})_2$), octacalcium phosphate (OCP, $\text{Ca}_8\text{H}_2(\text{PO}_4)_6 \cdot 5\text{H}_2\text{O}$) and whitlockite (WL, $\text{Ca}_{18}\text{Mg}_2(\text{HPO}_4)_2(\text{PO}_4)_{12}$)⁵³ within the so-called “*calcified aorta*”⁴². In a more recent study, *Rafael et al.* found that the XRD peaks of valvular calcifications matched those of stoichiometric HA, though a subset of experiment groups showed merging of the (211) and (112) peaks, indicative of carbonate substituting phosphate⁴³. XRD was also employed by my predecessors to characterize different regions of calcified aortic valves. Regions with moderate calcifications were found to be less crystalline, as evidenced by the poorer peak definition, when compared to regions with heavy calcifications, whereas regions with no visible calcifications exhibit diffraction patterns containing weak peaks that did not match any known apatite structure⁵⁴.

SEM provides morphologic and topographic information of sample surface via detection of emitted electrons⁵². SEM is often coupled with EDS, an elemental analysis technique via detection of emitted x-rays. *Bertazzo et al.* showed that calcifications in pathological aortic valves have multiple morphologies: “*dense spherical particles*”, “*dense*

fibers", and "*compact materials*"^{44,45}. A more recent study by *Gourgas et al.* confirmed the three distinctive structures⁴⁶. The spherical particles, according to electron diffraction patterns, tended to have a crystalline HA core and an amorphous outer layer, in which the former was found to be more crystalline and the latter less crystalline than the apatite in native bones⁴⁵. Moreover, *Prieto et al.* found via EDS that calcifications in aortic valves were composed primarily with Ca and P, with contributions from Mg, Na, K, and C⁴³. They also discerned two groups of mineral deposits: one with a low Ca/P ratio (1.59) that contained high Mg concentration and amorphous calcium phosphate, and the other with a high Ca/P ratio (1.89) that contained low Mg level and was composed predominantly of carbonated hydroxyapatite (CHA)⁴³. These preliminary results suggested that the mineralization in CAVD involves mechanisms other than osteogenesis.

Vibrational spectroscopy enables determination of organic and inorganic components based on detection of vibrational-rotational modes characteristic to functions groups and the associated environment. FTIR and Raman are two modalities of vibrational spectroscopy, where the former relies on the change in the dipole moment and the latter on the change in the molecular polarizability⁵⁵. Both modalities have demonstrated that most of the bioapatite in the human aortic valves is B-type CHA, where carbonate substitutes phosphate^{47,56}. FTIR spectra of both mineral and matrix species (e.g., collagen, elastin, and carbohydrates – components of GAGs) were collected within the human aortic valve⁴⁷. The FTIR analysis conducted by *Richards et al.* showed, from a small group of patients, that the bioapatite formed in the early-stage CAVD tends to have a lower crystallinity (i.e., a measure of size and perfection of crystals) and this crystallinity decreases with increasing carbonate to phosphate ratio⁵¹.

The study of bioapatite in the human aortic valve via Raman spectroscopy dates back to 1987 when *Clarke et al.* found that the mineral spectra of the aortic valve differed from those of the calcified coronary artery but resembled those of powdered CHA⁵⁷. *Pilarczyk et al.* found that larger-sized mineral deposits contained less carbonate when compared with smaller deposits⁴⁸. Recent studies proposed that the bioapatite in the aortic valve has multiple mineral phases (e.g., CHA and OCP)^{48,58}. Lipid species, such as fatty acids, cholesterol (with cholesteryl esters), phospholipids/triacylglycerols, and carotenoids, were also detected within the vicinity of mineral deposits^{50,58}.

1.3.2 Raman Signatures of Pathological Mineralization

Since Raman-active modes require an overall change in the molecular polarizability, i.e., a distortion of electrons away from their original positions, symmetric vibrational modes in general have stronger contributions to Raman spectra⁵⁵. For example, the symmetric stretching mode of phosphate ($\nu_1 \text{PO}_4^{3-}$) has a significantly stronger peak when compared to its asymmetric peer ($\nu_3 \text{PO}_4^{3-}$). Like many other spectroscopies, at least three important pieces of information can be extracted and exploited from a given peak in Raman:

- The **peak position** corresponds to the energy of a vibrational mode characteristic to a function group, along with the strain and general local environment.
- The **peak area**, or the integrated intensity, can provide a relative measure of the amount and scattering strength of the species in focus⁵⁹.
- The full width at half maximum (FWHM), also called as **peak width**, of phosphate peaks has been empirically validated against XRD results as a measure of apatite crystallinity⁶⁰.

Minerals

Vibrational modes of PO_4^{3-} , particularly symmetric stretching (ν_1), symmetric bending (ν_2), and asymmetric bending (ν_4), are often used as touchstones to validate and distinguish minerals from the organic matrix. The shift and appearance of $\nu_1 \text{PO}_4^{3-}$ can enable calcium phosphate mineral phase discrimination: unlike HA, pure or carbonated, whose $\nu_1 \text{PO}_4^{3-}$ peak at 960 cm^{-1} , both ACP and OCP have $\nu_1 \text{PO}_4^{3-}$ at lower wavenumbers, 952 cm^{-1} and 957 cm^{-1} , while both β -TCP and dicalcium phosphate dihydrate (DCPD) possess higher wavenumbers, 970 cm^{-1} and 985 cm^{-1} ^{48,61,62}. Since these peak positions were taken from synthetic calcium phosphate standards, the biogenic counterparts are likely to have altered $\nu_1 \text{PO}_4^{3-}$ peak positions. The potential causes might include but not limited to impurity inclusions and/or ionic substitutions, mineral-matrix (e.g., cells, ECM fibers) interactions, and mixing of multiple mineral phases.

A recent review paper by *Taylor & Donnelley* summarizes the primary bands assignments (Table 1.1) and key mineral-matrix parameters validated for Raman study on bone⁵⁵. Besides PO_4^{3-} , one anion that constructs the crystal lattice of OCP, brushite, (and even magnesium whitlockite) is acid phosphate (HPO_4^{2-}). The Raman peaks of HPO_4^{2-} lie within the vicinity of both ν_4 and $\nu_1 \text{PO}_4^{3-}$: P-OH stretching peaks at both $\sim 875 \text{ cm}^{-1}$ and $\sim 1000 \text{ cm}^{-1}$. However, since both signature peaks overlap with matrix species, the former with $\nu(\text{C}-\text{C})$ hydroxyproline and the latter $\nu(\text{C}-\text{C})$ phenylalanine, it can be extremely difficult, if not impossible, to separate pure HPO_4^{2-} from the rest in practice. Another anion prevalent in biogenic minerals is carbonate (CO_3^{2-}), especially in bone⁶³. The average carbonate content in healthy bones is about 6 wt.%. Carbonate can integrate into the crystal lattice by either being absorbed during crystal growth or substituting OH^- (type A), PO_4^{3-} (type B), and labile lattice

sites⁵⁵. Among the three, the peak of type B carbonate substitution at $\sim 1070\text{ cm}^{-1}$ is often found in biogenic minerals and is used to calculate relative carbonate content.

Matrix

Matrix is a generic term that summarizes the organic components of mineralized tissue. Therefore, matrix species include but are not limited to ECM proteins, lipids, and cells. The unique molecular structure of each species makes it distinguishable in Raman spectra. Before discussing the signature peaks of major matrix species, it is worthwhile to mention the commonality of spectral features they share.

The peptide bonds that link amino acids in proteins are readily detected using Raman. Two classic examples are Amide I, assigned as 80% C=O stretching at $1620\sim 1700\text{ cm}^{-1}$, and Amide III, assigned as 40% C-N stretching and 30% N-H bending at $1215\sim 1300\text{ cm}^{-1}$ ⁵⁵. Aromatic amino acids can also exhibit intense Raman peaks, e.g., phenylalanine has a sharp peak at $\sim 1000\text{ cm}^{-1}$, attributed to the ring deformation mode (ν_6)⁶⁴. Although the presence of these bands is largely determined by the vibrations of constituent functional groups, higher dimensional structures, e.g., tertiary and quaternary structures, along with the interactions between the amino acids in the side chains and the environment, e.g., hydrogen bonding⁶⁵ or elevated temperature⁶⁶, can dramatically change the size, shape, and position of the bands.

Structural proteins

The discussion on structural proteins is limited to collagen, elastin, and proteoglycans since they form the tri-layered structure of valvular ECM. Collagen has a long history of interaction with biogenic minerals. In bone growth, a highly regulated, multi-step process deposits matrix vesicles that contain mineral precursors like ACP into osteoid, forming hierarchically ordered, mineralized collagen fibrils⁴. Equally fascinating mineral-collagen arrangements can be traced in pathological mineralization. *Vidavsky & Kunitake* provide SEM

micrographs of, not only bone-like mineralized collagen fibrils in fibroadenoma, but also microcalcifications embedded within collagen fibrils in sclerosing adenosis (Figure 1.3)⁴. A similar scenario of minerals adjacent to a collagenous matrix was discovered and studied in Randall's plaque, precursors of renal stones⁶. The Raman spectra of most types of collagens share a similar but rather distinctive gestalt, characterized by two consecutive peak complexes at $\sim 874\text{ cm}^{-1}$ and $\sim 920\text{ cm}^{-1}$, attributed primarily to $\nu(\text{C-C})$ hydroxyproline and $\nu(\text{C-C})$ proline, and a third peak at $\sim 1242\text{ cm}^{-1}$, the first doublet peak of Amide III⁵⁵. In practice, the area ratio of two Amide III peaks, i.e., $1215\text{-}1300\text{ cm}^{-1}$ to $1300\text{-}1375\text{ cm}^{-1}$, can be used as a qualitative means to differentiate collagen from non-collagenous protein.

Table 1. 1. Primary Raman bands assignments on bone. The table explains the vibrational modes that attribute to the major Raman peaks for both mineral and matrix species in the spectral range of $400\text{-}1700\text{ cm}^{-1}$ (Reprinted from Ref. 55, with permission from Elsevier).

Vibrational mode	Underlying subband	Peak position/ integration range (cm^{-1})	Subband position (cm^{-1})	Comments	Reference
$\nu_2\text{ PO}_4^{3-}$		410–460 430			[36,98,99] [36,98]
$\nu_4\text{ PO}_4^{3-}$	$\nu_2\text{ PO}_4^{3-}$ shoulder	587	450	Contains contributions from acid phosphate (HPO_4) and octacalcium phosphate (OCP)	[36,98] [36,98]
$\nu(\text{C-C})$ Hydroxyproline	$\nu_4\text{ PO}_4^{3-}$ shoulder	604			[36,98]
P-OH		874		Isoleucine, valine, threonine, and tyrosine	[36,98]
$\nu(\text{C-C})$ Proline		879		Acid phosphate	[36,100]
$\nu_1\text{ PO}_4^{2-}$		920			[36,98]
		930–980			[97]
	$\nu_1\text{ PO}_4^{2-}$		960	Pure P–O stretch	[36,100]
	$\nu_1\text{ PO}_4^{2-}$		955	Immature bone mineral	[36,100]
	$\nu_1\text{ PO}_4^{2-}$		957–962	Mature bone mineral/carbonated apatite	[36,100]
$\nu(\text{C-C})$ phenylalanine		1003		Contains contributions from HPO_4 and $\nu_3\text{ PO}_4^{2-}$	[36,100,101]
Proteoglycan		1060		Contains overlap from phospholipids	[36,100,102]
$\nu_1\text{ CO}_3^{2-}$		1050–1100			[36,95]
	$\nu_1\text{ CO}_3^{2-} - \nu_2\text{ PO}_4^{2-}$		1030	CO_3 and PO_4 peaks not resolved	[95]
	$\nu_1\text{ CO}_3^{2-} - \nu_3\text{ PO}_4^{2-}$		1046	CO_3 and PO_4 peaks not resolved	[95]
	$\nu_3\text{ PO}_4^{2-}$		1076		[36,95]
Amide III		1215–1300			[36,99,103]
			1242	Doublet peak	[36,103]
			1272		[36,103]
Proteoglycan		1365–1390		Predominantly glycosaminoglycans	[99,102]
$\delta\text{ CH}_2$ lipids		1446		Contains contributions from proteins	[36,98]
Amide I		1620–1700			[97]
	predominantly irreducible pyridinoline crosslinks		1660	Requires second derivative spectroscopy and subband fitting.	[104]
	reducible divalent crosslinks		1690	Requires second derivative spectroscopy and subband fitting. Also requires further validation	[104]

Elastin is generally less studied in biomineralization compared to collagen. However, a recent study on atherosclerotic aortic tissues provides evidence of elastin-mineral (here apatite and whitlockite) colocalization, predominantly in tunica media⁶⁷. Elastin has also been found near a large calcification deposit in a calcified stenotic aortic valve via Raman

mapping⁵⁰. Although the Raman spectra of elastin and collagen resemble one another, elastin has a slightly different gestalt, characterized by a medium peak at $\sim 1108\text{ cm}^{-1}$, seemingly attributed to desmosine and isodesmosine (not fully confirmed), amino acids uniquely found in elastin, and another medium peak at $\sim 1340\text{ cm}^{-1}$, the second peak of Amide III⁶⁸.

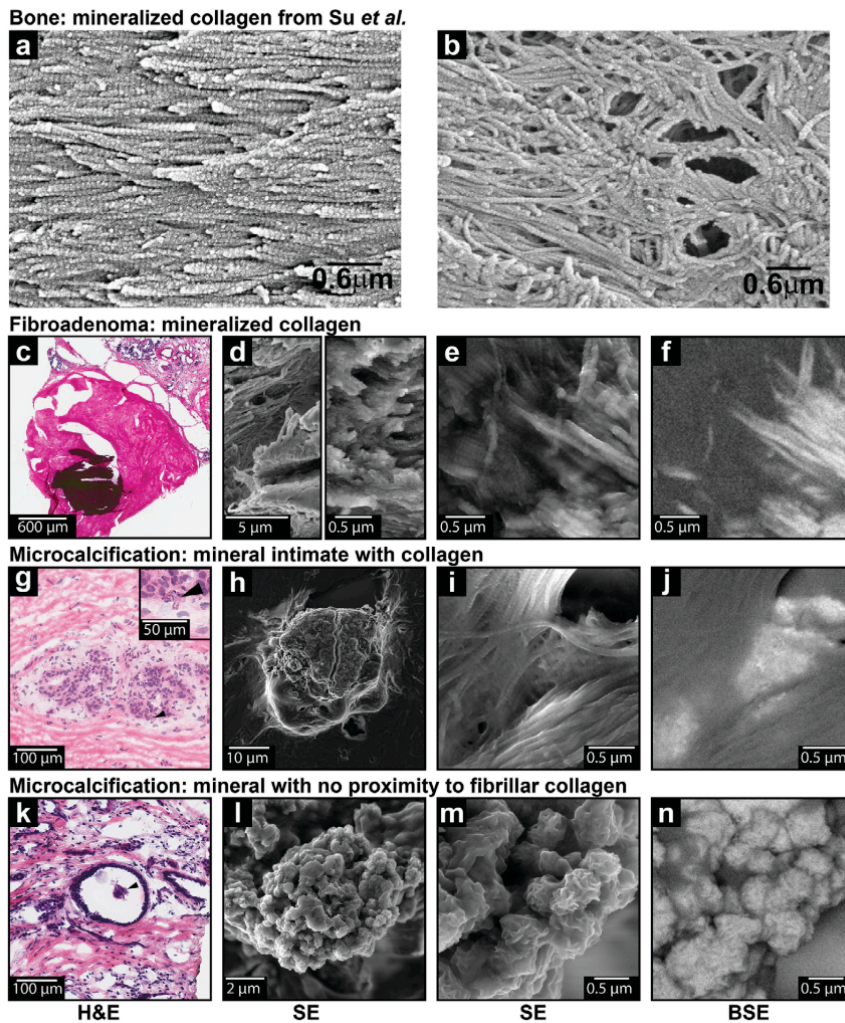


Figure 1. 3. The arrangements of minerals and collagen in both physiological and pathological mineralization. a, b). SEM images of mineralized collagen fibrils in human fetal bone. c-n). Both H&E-stained graphs and SEM images are shown for three representative breast cancer calcifications. c-f). Fibroadenoma. G-f). Sclerosing adenosis. k-n). Low-grade micropapillary pattern DCIS (Reprinted from Ref. 4, with permission from Wiley).

Proteoglycans are composed of a core protein and branched sugar side chains, namely glycosaminoglycans (GAGs). The loss of proteoglycans in the cartilage ECM has been identified as a feature of early-stage osteoarthritis. *Tianyu Gao* from the Estroff group applied Raman to map the distribution of chondroitin sulfate, a type of GAG, on an *in vitro* model that resembles osteoarthritis⁶⁹. Two spectral regions, i.e., 1000-1200 cm^{-1} and 1300-1450 cm^{-1} were identified as Raman signatures of GAGs. However, since both spectral regions overlap with other species – the former with carbonate & lipids and the latter with Amide III – detecting GAGs in biological mineral Raman spectra can be rather challenging in practice. FTIR might provide a viable solution, i.e., peak ratio of 1060 cm^{-1} to Amide I, for demineralized tissues, with spectral deconvolution and peak fitting^{55,70}.

Lipids

Lipids are another major matrix class present in calcified valvular tissues for reasons discussed in Ch. 1.2. Lipid Raman signatures stem mainly from their long, nonpolar hydrocarbon chains, so distinctive that they can be readily differentiated from other matrix species. In general, four spectral bands are shared among most lipids: C-C stretching (1050-1200 cm^{-1}), CH_2 twisting ($\sim 1300 \text{ cm}^{-1}$), CH_2/CH_3 scissoring (1400-1500 cm^{-1}), and C-H stretching (2800-3100 cm^{-1})⁷¹. Key Raman features of lipids species relevant to CAVD are discussed below. Readers interested in the Raman signatures of each lipid subclass are encouraged to find more details in the review paper by *Czamara et al.*⁷¹.

A fatty acid (FA) consists mainly of a monocarboxylic acid head group and a long hydrocarbon side chain. Besides the common signature aforementioned peaks, saturated fatty acids (SFAs) have two strong peaks at $\sim 1068 \text{ cm}^{-1}$ and $\sim 1120 \text{ cm}^{-1}$, both attributed to *trans* C-C stretching, and another two strong $\nu(\text{C-H})$ peaks at 2830-2890 cm^{-1} (C-H stretching in CH_2) and 2910-2970 cm^{-1} (C-H stretching in CH_3)⁶⁴. Meanwhile, the additional C=C double

bond(s) present in unsaturated fatty acids (UFAs) is/are reflected in Raman spectra. The *trans* C-C stretching peaks ($\sim 1068\text{ cm}^{-1}$ and $\sim 1230\text{ cm}^{-1}$) are less intense, due to the discontinuation of C-C long chain by C=C double bond(s), and partially replaced by a peak at $\sim 1086\text{ cm}^{-1}$, attributed to *gauche* C-C stretching vibration. The CH_2 twisting peak at $\sim 1300\text{ cm}^{-1}$ is also lowered and becomes a doublet peak for similar reasons. Instead, the presence of C=C double bond(s) provides UFAs with several new vibrational modes, i.e., =C-H deformation peak at $\sim 1260\text{ cm}^{-1}$, C=C stretching peak at $\sim 1665\text{ cm}^{-1}$, and =C-H stretching peak at $\sim 3000\text{ cm}^{-1}$ ⁷¹.

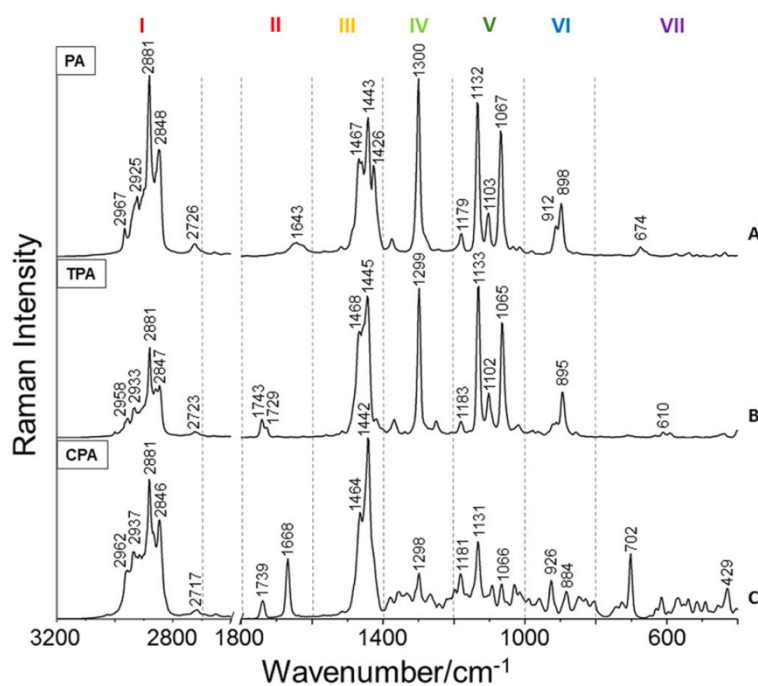


Figure 1. 4. Raman spectra of three representative lipid species. A). Saturated fatty acids like palmitic acid have a characteristic peak complex at region III. B). Triacylglycerols have a characteristic peak at 1740 cm^{-1} , assigned to the ester bond. C). Cholesterol esters can be discerned from peaks at 429 cm^{-1} and 702 cm^{-1} , assigned to the backbone vibrational mode (Reprinted from Ref. 71, with permission from Wiley).

Since FAs are essential building blocks of triacylglycerols (TAGs), it is not surprising that the latter shares similar Raman signatures with their corresponding FAs. What distinguishes TAGs from other lipid species is the C=O stretching of the ester group: 1730-

1750 cm^{-1} for TAGs versus $\sim 1650 \text{ cm}^{-1}$ for FAs⁷¹. Such a difference was primarily due to replacement of the carboxylic acid group with an ester group. Furthermore, cholesterol have characteristic peaks at $\sim 430 \text{ cm}^{-1}$ and $\sim 700 \text{ cm}^{-1}$, both attributed to the backbone vibration modes. An additional C=O stretching peak at $\sim 1740 \text{ cm}^{-1}$ is often used to distinguish cholesteryl ester from pure cholesterol⁷². Last, phospholipids have a characteristic peak at $\sim 1090 \text{ cm}^{-1}$, attributed to P-O stretching vibration, while the attached head groups also have distinctive peaks, such as $\sim 720 \text{ cm}^{-1}$ for choline and $\sim 760 \text{ cm}^{-1}$ for ethanolamine⁷¹.

Cells

Cells, in this case VIC and VEC, play an indispensable role in both maintaining valvular homeostasis and exacerbating valvular calcification. Raman can be used to distinguish cells from the rest of the matrix proteins, mostly via the fingerprints of DNA/RNA. A peak complex at 780-800 cm^{-1} is assigned to the stretching vibration of the O-P-O backbone, along with the ring breathing modes of pyrimidines, i.e., C, T, and U⁷³. A peak at $\sim 1575 \text{ cm}^{-1}$ is attributed to the ring breathing modes of purines, i.e., G, A^{73,74}. Pyrimidines have another ring breathing mode around 1665-1680 cm^{-1} , though in practice it overlaps with the generic protein peak of Amide I^{74,75}. Readers interested in the full profile of Raman cell signatures are advised to find more details in the review paper by *Chan et al.*⁷⁵.

1.4 Summary and Outlook

The chapter begins with a broad overview on the field of biomineralization, introducing two main categories of biomineralization: physiological and pathological mineralization (Ch. 1.1). CAVD falls into the category of pathological mineralization. To understand the root cause, this narrative dives into the anatomy of the aortic valve, discusses the epidemiology of CAVD (e.g., symptoms, progressions, and treatment options),

and decomposes the major events in the progression of CAVD: endothelial dysfunction, chronic inflammation, fibrosis, and mineralization (Ch. 1.2). The focus is then shifted to biomineralization and materials science, summarizing three characterization techniques that have been applied to study valvular calcification. Among the three, Raman spectroscopy is explored thoroughly, where recent findings and peak assignments of both mineral and matrix species (i.e., structural proteins, lipids, and cells) are explained in detail (Ch. 1.3).

In the next chapter, Raman microscopy is applied to characterize valvular calcifications in human tissue samples (Ch. 1.3). The hyperspectral data sets are then processed to explore the heterogeneity of matrix-mineral relationships (Ch. 1.2), and when combined with patient clinical data, to provide insights on the underlying biomineralization pathways (Ch. 1.1).

REFERENCES

1. Lowenstam HA, Weiner S. *On Biomineralization*. Oxford University Press on Demand; 1989.
2. Elliott JC. *Structure and Chemistry of the Apatites and Other Calcium Orthophosphates*. Elsevier; 2013.
3. Reznikov N, Hoac B, Buss DJ, Addison WN, Barros NMT, McKee MD. Biological stenciling of mineralization in the skeleton: Local enzymatic removal of inhibitors in the extracellular matrix. *Bone*. 2020;138:115447.
4. Vidavsky N, Kunitake JAMR, Estroff LA. Multiple Pathways for Pathological Calcification in the Human Body. *Advanced Healthcare Materials*. Published online December 4, 2020:2001271. doi:10.1002/adhm.202001271
5. Kunitake JAMR, Choi S, Nguyen KX, et al. Correlative imaging reveals physiochemical heterogeneity of microcalcifications in human breast carcinomas. *Journal of Structural Biology*. 2018;202(1):25-34. doi:10.1016/j.jsb.2017.12.002
6. Gay C, Letavernier E, Verpont M-C, et al. Nanoscale Analysis of Randall's Plaques by Electron Energy Loss Spectromicroscopy: Insight in Early Biomineral Formation in Human Kidney. *ACS Nano*. 2020;14(2):1823-1836. doi:10.1021/acsnano.9b07664
7. Driscoll K, Cruz AD, Butcher JT. Inflammatory and Biomechanical Drivers of Endothelial-Interstitial Interactions in Calcific Aortic Valve Disease. *Circulation Research*. Published online 2021:1344-1370. doi:10.1161/CIRCRESAHA.121.318011
8. Vyas P, Hutcheson JD, Aikawa E. Calcific Aortic Valve Disease: Pathobiology, Basic Mechanisms, and Clinical Strategies. *Advances in Heart Valve Biomechanics*. Published online 2018:153-179. doi:10.1007/978-3-030-01993-8
9. Kostyunin AE, Yuzhalin AE, Ovcharenko EA, Kutikhin AG. Development of calcific aortic valve disease: Do we know enough for new clinical trials? *Journal of Molecular and Cellular Cardiology*. 2019;132(May):189-209. doi:10.1016/j.yjmcc.2019.05.016
10. Sacks MS, Liao J. *Advances in Heart Valve Biomechanics: Valvular Physiology, Mechanobiology, and Bioengineering*. Springer; 2018.

11. Yutzey KE, Demer LL, Body SC, et al. Calcific aortic valve disease: A consensus summary from the alliance of investigators on calcific aortic valve disease. *Arteriosclerosis, Thrombosis, and Vascular Biology*. 2014;34(11):2387-2393. doi:10.1161/ATVBAHA.114.302523
12. Lindman BR, Clavel MA, Mathieu P, et al. Calcific aortic stenosis. *Nature Reviews Disease Primers*. 2016;2. doi:10.1038/nrdp.2016.6
13. Danielsen R, Aspelund T, Harris TB, Gudnason V. The prevalence of aortic stenosis in the elderly in Iceland and predictions for the coming decades: the AGES-Reykjavík study. *International journal of cardiology*. 2014;176(3):916-922. doi:10.1016/j.ijcard.2014.08.053
14. Baron SJ, Wang K, House JA, et al. Cost-Effectiveness of Transcatheter Versus Surgical Aortic Valve Replacement in Patients with Severe Aortic Stenosis at Intermediate Risk: Results from the PARTNER 2 Trial. *Circulation*. 2019;139(7):877-888. doi:10.1161/CIRCULATIONAHA.118.035236
15. Virani SS, Alonso A, Benjamin EJ, et al. *Heart Disease and Stroke Statistics—2020 Update: A Report from the American Heart Association.*; 2020. doi:10.1161/CIR.0000000000000757
16. Poggianti E, Venneri L, Chubuchny V, Jambrik Z, Baroncini LA, Picano E. Aortic valve sclerosis is associated with systemic endothelial dysfunction. *Journal of the American College of Cardiology*. 2003;41(1):136-141. doi:10.1016/S0735-1097(02)02622-0
17. Butcher JT, Nerem RM. Valvular endothelial cells and the mechanoregulation of valvular pathology. *Philosophical Transactions of the Royal Society B: Biological Sciences*. 2007;362(1484):1445-1457. doi:10.1098/rstb.2007.2127
18. Hoehn D, Sun L, Sucosky P. Role of Pathologic Shear Stress Alterations in Aortic Valve Endothelial Activation. *Cardiovascular Engineering and Technology*. 2010;1(2):165-178. doi:10.1007/s13239-010-0015-5
19. Sucosky P, Balachandran K, Elhammali A, Jo H, Yoganathan AP. Altered shear stress stimulates upregulation of endothelial VCAM-1 and ICAM-1 in a BMP-4- and TGF- β 1-dependent pathway. *Arteriosclerosis, Thrombosis, and Vascular Biology*. 2009;29(2):254-260. doi:10.1161/ATVBAHA.108.176347
20. Hutcheson JD, Aikawa E, Merryman WD. Potential drug targets for calcific aortic valve

- disease. *Nature Reviews Cardiology*. 2014;11(4):218-231.
doi:10.1038/nrcardio.2014.1
21. Osman N, Grande-Allen KJ, Ballinger ML, et al. Smad2-dependent glycosaminoglycan elongation in aortic valve interstitial cells enhances binding of LDL to proteoglycans. *Cardiovascular Pathology*. 2013;22(2):146-155. doi:10.1016/j.carpath.2012.07.002
 22. Yetkin E, Waltenberger J. Molecular and cellular mechanisms of aortic stenosis. *International Journal of Cardiology*. 2009;135(1):4-13.
doi:10.1016/j.ijcard.2009.03.108
 23. Šteiner I, Stejskal V, Žáček P. Mast cells in calcific aortic stenosis. *Pathology Research and Practice*. 2018;214(1):163-168. doi:10.1016/j.prp.2017.07.016
 24. Merryman WD, Lukoff HD, Long RA, Engelmayr GC, Hopkins RA, Sacks MS. Synergistic effects of cyclic tension and transforming growth factor- β 1 on the aortic valve myofibroblast. *Cardiovascular Pathology*. 2007;16(5):268-276.
doi:10.1016/j.carpath.2007.03.006
 25. Chen JH, Chen WLK, Sider KL, Yip CYY, Simmons CA. B-Catenin Mediates Mechanically Regulated, Transforming Growth Factor-B1-Induced Myofibroblast Differentiation of Aortic Valve Interstitial Cells. *Arteriosclerosis, Thrombosis, and Vascular Biology*. 2011;31(3):590-597. doi:10.1161/ATVBAHA.110.220061
 26. Edep ME, Shirani J, Wolf P, Brown DL. Matrix metalloproteinase expression in nonrheumatic aortic stenosis. *Cardiovascular Pathology*. 2000;9(5):281-286.
doi:10.1016/S1054-8807(00)00043-0
 27. Fondard O, Detaint D, Iung B, et al. Extracellular matrix remodelling in human aortic valve disease: The role of matrix metalloproteinases and their tissue inhibitors. *European Heart Journal*. 2005;26(13):1333-1341. doi:10.1093/eurheartj/ehi248
 28. Helske S, Syväranta S, Lindstedt KA, et al. Increased expression of elastolytic cathepsins S, K, and V and their inhibitor cystatin C in stenotic aortic valves. *Arteriosclerosis, Thrombosis, and Vascular Biology*. 2006;26(8):1791-1798.
doi:10.1161/01.ATV.0000228824.01604.63
 29. Helske S, Lindstedt KA, Laine M, et al. Induction of local angiotensin II-producing systems in stenotic aortic valves. *Journal of the American College of Cardiology*. 2004;44(9):1859-1866. doi:10.1016/j.jacc.2004.07.054

30. O'Brien KD, Shavelle DM, Caulfield MT, et al. Association of angiotensin-converting enzyme with low-density lipoprotein in aortic valvular lesions and in human plasma. *Circulation*. 2002;106(17):2224-2230. doi:10.1161/01.CIR.0000035655.45453.D2
31. Soini Y, Salo T, Satta J. Angiogenesis is involved in the pathogenesis of nonrheumatic aortic valve stenosis. *Human Pathology*. 2003;34(8):756-763. doi:10.1016/S0046-8177(03)00245-4
32. Syväranta S, Helske S, Laine M, et al. Vascular endothelial growth factor-secreting mast cells and myofibroblasts: A novel self-perpetuating angiogenic pathway in aortic valve stenosis. *Arteriosclerosis, Thrombosis, and Vascular Biology*. 2010;30(6):1220-1227. doi:10.1161/ATVBAHA.109.198267
33. Cottignoli V, Relucenti M, Agrosi G, et al. Biological Niches within Human Calcified Aortic Valves: Towards Understanding of the Pathological Biomineralization Process. *BioMed Research International*. 2015;2015. doi:10.1155/2015/542687
34. Rajamannan NM, Sangiorgi G, Springett M, et al. Experimental hypercholesterolemia induces apoptosis in the aortic valve. *Journal of Heart Valve Disease*. 2001;10(3):371-374.
35. Laird DF, Mucalo MR, Yokogawa Y. Growth of calcium hydroxyapatite (Ca-HAp) on cholesterol and cholestanol crystals from a simulated body fluid: A possible insight into the pathological calcifications associated with atherosclerosis. *Journal of Colloid and Interface Science*. 2006;295(2):348-363. doi:10.1016/j.jcis.2005.09.013
36. Liu X, Xu Z. Osteogenesis in calcified aortic valve disease: From histopathological observation towards molecular understanding. *Progress in Biophysics and Molecular Biology*. 2016;122(2):156-161. doi:10.1016/j.pbiomolbio.2016.02.002
37. Mathieu P, Boulanger MC. Basic mechanisms of calcific aortic valve disease. *Canadian Journal of Cardiology*. 2014;30(9):982-993. doi:10.1016/j.cjca.2014.03.029
38. Simionescu A, Simionescu DT, Vyavahare NR. Osteogenic Responses in Fibroblasts Activated by Elastin Degradation Products and Transforming Role of Myofibroblasts in Vascular Calcification. *The American Journal of Pathology*. 2007;171(1):116-123. doi:10.2353/ajpath.2007.060930
39. Gee, T.W. (2020) Coregulatory mechanisms of cellular recruitment in fibrocalcific aortic valve disease [Doctoral dissertation, Conrell University, Ithaca].

40. Dweck MR, Jenkins WSA, Vesey AT, et al. ¹⁸F-Sodium Fluoride Uptake Is a Marker of Active Calcification and Disease Progression in Patients With Aortic Stenosis. *Circulation: Cardiovascular Imaging*. 2014;7(2):371-378. doi:10.1161/CIRCIMAGING.113.001508
41. Jung JJ, Jadbabaie F, Sadeghi MM. Molecular imaging of calcific aortic valve disease. *Journal of Nuclear Cardiology*. 2018;25(4):1148-1155. doi:10.1007/s12350-017-1158-7
42. Höhling H. The mineral components in aortic "calcification" studied by x-ray and electron diffraction combined with electron microscopy. *German medical monthly*. 1968;13(3):135-138.
43. Prieto RM. Study on the structure and composition of aortic valve calcific deposits. etiological aspects. *Journal of Biophysical Chemistry*. 2011;02(01):19-25. doi:10.4236/jbpc.2011.21003
44. Bertazzo S, Gentleman E. Aortic valve calcification: a bone of contention. *European Heart Journal*. 2017;38:1189-1193. doi:10.1093/eurheartj/ehw071
45. Bertazzo S, Gentleman E, Cloyd KL, Chester AH, Yacoub MH, Stevens MM. Nano-analytical electron microscopy reveals fundamental insights into human cardiovascular tissue calcification. *Nature Materials*. 2013;12(6):576-583. doi:10.1038/nmat3627
46. Gourgas O, Khan K, Schwertani A, Cerruti M. Differences in mineral composition and morphology between men and women in aortic valve calcification. *Acta Biomaterialia*. 2020;106:342-350. doi:10.1016/j.actbio.2020.02.030
47. Jastrzebska M, Zalewska-Rejda J, Mróz I, et al. Atomic force microscopy and FT-IR spectroscopy investigations of human heart valves. *General physiology and biophysics*. 2006;25:231-244.
48. Pilarczyk M, Czamara K, Baranska M, et al. Calcification of aortic human valves studied in situ by Raman microimaging: Following mineralization from small grains to big deposits. *Journal of Raman Spectroscopy*. 2013;44(9):1222-1229. doi:10.1002/jrs.4352
49. Czamara K, Natarska J, Kapusta P, Baranska M, Kaczor A. Raman microspectroscopy of human aortic valves: Investigation of the local and global biochemical changes associated with calcification in aortic stenosis. *Analyst*. 2015;140(7):2164-2170.

doi:10.1039/c4an01856g

50. Bonetti A, Bonifacio A, della Mora A, Livi U, Marchini M, Ortolani F. Carotenoids co-localize with hydroxyapatite, cholesterol, and other lipids in calcified stenotic aortic valves. Ex vivo Raman maps compared to histological patterns. *European Journal of Histochemistry*. 2015;59(2):93-97. doi:10.4081/ejh.2015.2505
51. Richards JM, Kunitake JAMR, Hunt HB, et al. Crystallinity of hydroxyapatite drives myofibroblastic activation and calcification in aortic valves. *Acta Biomaterialia*. 2018;71:24-36. doi:10.1016/j.actbio.2018.02.024
52. Skoog DA, Holler FJ, Crouch SR. *Instrumental Analysis*. Vol 47. Brooks/Cole, Cengage Learning Belmont; 2007.
53. Shah FA. Magnesium whitlockite – omnipresent in pathological mineralisation of soft tissues but not a significant inorganic constituent of bone. *Acta Biomaterialia*. 2021;125:72-82. doi:10.1016/j.actbio.2021.02.021
54. Richards, J.M. (2015). Endothelial regulation of valve interstitial cells in calcific aortic valve disease. [Doctoral dissertation, Cornell University, Ithaca]. doi:10.1145/3132847.3132886
55. Taylor EA, Donnelly E. Raman and Fourier transform infrared imaging for characterization of bone material properties. *Bone*. 2020;139(May). doi:10.1016/j.bone.2020.115490
56. Pilarczyk M, Czamara K, Baranska M, et al. Calcification of aortic human valves studied in situ by Raman microimaging: Following mineralization from small grains to big deposits. *Journal of Raman Spectroscopy*. 2013;44(9):1222-1229. doi:10.1002/jrs.4352
57. Clarke RH, Hanlon EB, Isner JM, Brody H. Laser Raman spectroscopy of calcified atherosclerotic lesions in cardiovascular tissue. *Applied Optics*. 1987;26(16):3175. doi:10.1364/AO.26.003175
58. Czamara K, Natarska J, Kapusta P, Baranska M, Kaczor A. Raman microspectroscopy of human aortic valves: Investigation of the local and global biochemical changes associated with calcification in aortic stenosis. *Analyst*. 2015;140(7):2164-2170. doi:10.1039/c4an01856g

59. Dieing T, Hollricher O, Toporski J, eds. *Confocal Raman Microscopy*. Vol 158. Springer Berlin Heidelberg; 2011. doi:10.1007/978-3-642-12522-5
60. Kazanci M, Fratzl P, Klaushofer K, Paschalis EP. Complementary information on in vitro conversion of amorphous (precursor) calcium phosphate to hydroxyapatite from raman microspectroscopy and wide-angle X-ray scattering. *Calcified Tissue International*. 2006;79(5):354-359. doi:10.1007/s00223-006-0011-9
61. Stewart S, Shea DA, Tarnowski CP, et al. Trends in early mineralization of murine calvarial osteoblastic cultures: A Raman microscopic study. *Journal of Raman Spectroscopy*. 2002;33(7):536-543. doi:10.1002/jrs.892
62. Sauer GR, Zunic WB, Durig JR, Wuthier RE. Fourier transform raman spectroscopy of synthetic and biological calcium phosphates. *Calcified Tissue International*. 1994;54(5):414-420. doi:10.1007/BF00305529
63. Paschalis EP, Gamsjaeger S, Klaushofer K. Vibrational spectroscopic techniques to assess bone quality. *Osteoporosis International*. 2017;28(8):2275-2291. doi:10.1007/s00198-017-4019-y
64. Miller FA. Misassignment of the strong Raman band near 1000 cm^{-1} in some substituted benzenes, and the Herzberg versus Wilson convention for numbering the vibrations of benzene. *Journal of Raman Spectroscopy*. 1988;19(3):219-221. doi:10.1002/jrs.1250190313
65. Harper ET, Rose GD. Helix stop signals in proteins and peptides: the capping box. *Biochemistry*. 1993;32(30):7605-7609.
66. Dong R, Yan X, Pang X, Liu S. Temperature-dependent Raman spectra of collagen and DNA. *Spectrochimica Acta - Part A: Molecular and Biomolecular Spectroscopy*. 2004;60(3):557-561. doi:10.1016/S1386-1425(03)00262-2
67. You AYP, Bergholt MS, St-Pierre J-P, et al. Raman spectroscopy imaging reveals interplay between atherosclerosis and medial calcification in the human aorta. *Science Advances*. 2017;3(12):e1701156. doi:10.1126/sciadv.1701156
68. Frushour BG, Koenig JL. Raman scattering of collagen, gelatin, and elastin. *Biopolymers*. 1975;14(2):379-391. doi:10.1002/bip.1975.360140211

69. Gao, T. (2020). Non-Destructive Spatial Mapping of GAG Loss in Articular Cartilage Using Confocal Raman Spectroscopy [Master's thesis, Cornell University, Ithaca].
70. Rieppo L, Rieppo J, Jurvelin JS, Saarakkala S. Fourier transform infrared spectroscopic imaging and multivariate regression for prediction of proteoglycan content of articular cartilage. *PLoS ONE*. 2012;7(2). doi:10.1371/journal.pone.0032344
71. Czamara K, Majzner K, Pacia MZ, Kochan K, Kaczor A, Baranska M. Raman spectroscopy of lipids: a review. *Journal of Raman Spectroscopy*. 2015;46(1):4-20. doi:10.1002/jrs.4607
72. Krafft C, Neudert L, Simat T, Salzer R. Near infrared Raman spectra of human brain lipids. *Spectrochimica Acta - Part A: Molecular and Biomolecular Spectroscopy*. 2005;61(7):1529-1535. doi:10.1016/j.saa.2004.11.017
73. Movasaghi Z, Rehman S, Rehman IU. Raman Spectroscopy of Biological Tissues. *Applied Spectroscopy Reviews*. 2007;42(5):493-541. doi:10.1080/05704920701551530
74. Vidavsky N, Kunitake JAMR, Diaz-Rubio ME, et al. Mapping and Profiling Lipid Distribution in a 3D Model of Breast Cancer Progression. *ACS Central Science*. 2019;5(5):768-780. doi:10.1021/acscentsci.8b00932
75. Chan JW, Taylor DS, Zwerdling T, Lane SM, Ihara K, Huser T. Micro-Raman spectroscopy detects individual neoplastic and normal hematopoietic cells. *Biophysical Journal*. 2006;90(2):648-656. doi:10.1529/biophysj.105.066761

CHAPTER 2
MAPPING AND PROFILING THE HETEROGENEITY OF CALCIFICATIONS IN DISEASED
HUMAN AORTIC VALVES

2.1 Introduction

The human aortic valve is a thin, avascular tissue that resides at the aortic root. The main function of the aortic valve is to facilitate unidirectional blood flow through the heart and to prevent regurgitation during systole-diastole cycle¹. However, the homeostasis of the aortic valve is no longer maintained during calcific aortic valve disease (CAVD), characterized by fibro-calcific remodeling of the valve leaflets that obstruct blood flow². Though the true cause of CAVD remains elusive, endothelial injury is widely acknowledged as the trigger². The dysfunction of the endothelial lining allows lipids to infiltrate and accumulate within the leaflets, triggering inflammation and maladaptive remodeling of valvular ECM². The synthesis of new structural proteins and degradation of the old, mature ones, coupled with mineral growth, thicken and stiffen the valve leaflets, leading to symptoms including but not limited to heart failure, angina, and syncope³. Echocardiography is the primary diagnostic tool to date, and valve replacement surgeries at late-stage CAVD remain to be the only effective treatment.

To develop therapeutic strategies that can either relieve the symptoms or diagnose CAVD at earlier stages require a deeper understanding of its pathobiology. The emphasis has long been a top-down approach. Tremendous progress has been made on developing both *in vitro* and *in vivo* systems that mimic the risk factors associated with CAVD. *Richards et al.* implemented a 3D coculture of VICs and VECs to study the cellular response in calcification-prone environments, i.e., osteogenic, mineralized, and mechanical environments⁴. *Gee et al.*

further developed the coculture systems to study VEC-VIC interactions, i.e., endothelial to mesenchymal transition (EndMT), and cellular signaling, e.g., canonical NF κ B and Notch1 pathways⁵. Such a top-down approach has already yielded some fruits. For example, the canonical NF κ B pathway (via IKK β silencing) was identified as a potential therapeutic target both *in vitro* and *in vivo*.

However, there are missing pieces to the puzzle. The intrinsic limitation of all biological assays, *in vitro* or *in vivo*, prevents one from fully recapitulating both pathological environment and disease progression of CAVD. *Gee et al.* pointed out that in a murine model no sex-specific differences of the minerals were ever found and assigned the cause of which to “*the early timepoint of assessment*”⁵. The top-down approach underscores the interplay of cell signaling pathways and maladaptive remodeling of the valvular ECM thought to be early events in disease progression. The mineral end products that so define CAVD may also provide therapeutically relevant information or potentially encapsulate details linked to pathogenesis. However, this type of analysis is made difficult by the inherent heterogeneity of biological samples and a lack of appropriate characterization tools. Common techniques employed in biological studies, e.g., Western blots, immunofluorescence, polymerase chain reactions, etc., target mostly on cellular proteins and DNAs, rarely on biogenic minerals. Computed tomography and histology are the main techniques used to differentiate high-density, calcium-phosphate complexes from the tissue, but the associated gradient/color-based results can only affirm the presence of biogenic minerals and fall short of determining either structure or property of the minerals.

The aim of this study is to fill in a missing piece of the puzzle via a bottom-up approach. By incorporating materials science into translational medicine, the study explores the biogenic minerals of surgically excised patient aortic valves via Raman microscopy, which

enables mapping and characterization of minerals and organic components. This scheme is not new, but most previous works put emphasis solely on the biogenic minerals⁶⁻⁸. Since cells secrete proteins to form the extracellular matrix (ECM) and the latter is closely associated with the growth of biogenic minerals, elucidating the interplay between mineral and matrix components helps to uncover the underlying mechanisms of mineral formation. In this study, the heterogeneous distributions of both mineral and matrix species are explored through hyperspectral data analysis of Raman mapping. A hierarchical clustering is then built to visualize the fingerprints of biogenic minerals and trace potential patterns that explain the biomineralization pathways of valvular calcification.

2.2 Materials and Methods

2.2.1 Human aortic valve samples

Human diseased aortic valve samples (n = 21) were provided by the Butcher group (Figure A.1). The valves were excised from adult patients undergoing valve replacement surgery by Dr. Sanjay Samy at the Robert Packer Hospital (Sayer, PA)⁴⁸. All procedures were approved by the Institutional Review Board at Cornell University and the Guthrie Clinic⁴⁸. The valves were retrieved directly from the operating room, transported to the lab in PBS, and fixed in 4% paraformaldehyde overnight⁴⁸. More details about tissue processing were documented in *Dr. Richards' thesis*⁵¹. The fixed valves were then stored in 70% ethanol and photographed to inspect regions of macro-calcifications.

2.2.2 Micro-CT scanning, model generations, and index sum scoring

A total of 21 excised valve samples from 20 patients were loaded into three centrifuge tubes and scanned using X-ray microtomography, or micro-CT (Bruker Skyscan

1276). Styrofoam was cut and inserted into tubes to prevent physical contact between two adjacent valve samples. After preparation, the tubes, along with two calibration phantoms, were installed into a stationary sample holder. The samples then absorbed x-ray signals from a rotating emitter and reflected them to a rotating detector. The x-ray was emitted with a source voltage of 85 kV and a power of 17 W. A rotation step of 0.4 degree was performed for a full 360-degree rotation, with a resolution of 20 $\mu\text{m}/\text{pixel}$, a depth of 16 bits, and an exposure time of 460 ms (or 480 ms) (Note: micro-CT scanning was operated by *Dr. Teresa Perri* from Cornell BRC imaging facility).

3D rendering of these patient valve samples was carried out by processing z-stacked images in Avizo software to visualize soft tissues and calcifications (Figure A.1). After calibrating the micro-CT data based on the two phantoms with known density (i.e., 0.25 g/cc and 0.75 g/cc), a thresholding technique was applied to set the range of CT numbers into five groups: soft tissue, light calcification, medium calcification, heavy calcification, and extremely heavy calcification. Voxels with the associated CT numbers were assigned to the corresponding color-coded group.

Index sum scoring was applied to quantify the level of valvular calcification. Each group was assigned with an index number: soft tissue: 0, light calcification: 1, medium calcification: 2, heavy calcification: 3, and extremely heavy calcification: 4. The products of voxels in each group and the corresponding index number were then summed to generate a score to quantitatively measure the level of calcification of each valve sample.

2.2.3 Sample preparation and histology.

A total of 13 valve samples (from 13 patients) were selected for further investigation, for reasons including but not limited to continuous micro-CT scoring, sample validity (e.g., no

myocardial wall attachment), time, and budget. Those 13 valves were further divided into two groups and processed separately. According to the micro-CT scores, the less mineralized valve samples (N = 4) were sent to the histology lab in Cornell University College of Veterinary Medicine for cryosection. Meanwhile, the more mineralized valve samples (n = 9) were shipped to the histology lab in Yale School of Medicine and embedded in polymethyl methacrylate (PMMA). All samples were embedded at designated orientations and sectioned at 5 μm (except a 1.5 μm section for FTIR). Two serial sections were stained with von Kossa and Movat Pentachrome, to depict minerals and tissue architecture, and a third was reserved for Raman analysis (Figure A.3). All sections were later retrieved from histology labs and preserved at the Estroff lab for histological and spectroscopical analyses. The stained slides were imaged via a ScanScope (Aperio CS2, Leica Biosystems) with a 40x objective from the Stem Cell Pathology Unit.

2.2.4 Raman data collection

A confocal Raman microscope (Alpha300R, WITec) with a 532 nm laser excitation source was used. The diffraction gratings of the spectrometer were adjusted to 300 l/mm, which corresponded to a spectral resolution of $\sim 3 \text{ cm}^{-1}$. The spectral center was assigned to 1600 cm^{-1} to fully encompass both the mineral and the C-H stretching complex. After calibrating on the Si wafer, valve sections (N = 10) were placed on a motorized stage and imaged via a 5x objective (Zeiss, 0.25 NA). The regions of interest (ROIs) were then carefully determined by comparing white-light graphs with the corresponding von Kossa images.

For each ROI, a higher-resolution, white-light image was first taken using a 50x objective (Zeiss, 0.55 NA). Several “point and shoot” Raman spectra were then collected with a laser power of 15-20 mW (15 mW for most cases) and a total integration time of 45-60 s

(unit integration time: 1 s, accumulations: 45-60) to confirm the presence of minerals.

Calcification regions with poor signals or intense fluorescence were excluded.

“True surface” mode was turned on to enable auto-focusing during large-area scans (focus shift: 5.00, min. signal: 1.30%, feedback p-gain & l-gain: 0.00). Several variables (e.g., length, width, resolution, and angle) were inputted to define the geometry of the mapping regions. Though mapping size could vary, the resolution was set to $0.8 * 0.8 \text{ um}^2$, with a laser power of 13-18 mW (15 mW for most cases) and an integration time of 0.5-1 s per pixel (0.75 for most cases). For regions that had mild fluorescence, photobleaching was performed manually by clicking on the pixels inside the selected regions and holding for a period in the oscilloscope mode prior to large-area scanning.

2.2.5 Raman combinational maps

Prior to any analysis, the collected Raman data were processed using WITec Project FIVE+. All spectra were first calibrated (i.e., Rayleigh peak = 0.00 cm^{-1}). The spectral range was cropped to 79-969 pixels ($320\text{-}3795 \text{ cm}^{-1}$) and the background was subtracted using a “shape” function (shape size = 100). For hyperspectral datasets, cosmic rays were removed automatically via the CRR tab (filter size = 4, dynamic factor = 8). Such a four-step process ensured clean, smooth spectra ready for data analysis.

A combinational map was generated from each of the selected hyperspectral datasets to visualize mineral and matrix species simultaneously. Three methods were employed to make combinational maps via the WITec software: filters, true component analysis (TCA), and non-negative matrix factorization (NMF). The fundamental principle behind the three is shared, where a color-coded heat map of each component either displays the integration of a chemically characteristic band area at each spatial pixel (i.e., filters) or

displays the quantified spectral contribution at each pixel based on multivariate analyses (i.e., TCA & NMF). Heat maps for different components were overlaid onto one another to produce the combinational map.

In this study, a combination of all three techniques were employed to generate high-quality combinational maps. Filters were first applied to assess the mineral-matrix components. TCA was followed to both determine the number of bases and manually mask out pixels contaminated by cosmic rays. Both the number of bases (often 5-7) and the clean hyperspectral dataset were input into the NMF, an unsupervised program that decomposes the hyperspectral dataset into spectral bases and bases maps. Only biologically relevant bases were selected, and the associated maps overlaid to generate the final combinational map.

2.2.6 Mean Raman spectra and statistical analysis

A mean spectrum was extracted from each of the selected hyperspectral dataset to represent that calcification of interest. Masks were generated to exclude pixels that were devoid of calcification, often by thresholding the ratios of two filter results. Two generic masks were applied to all calcification regions of interest, i.e., noise to signal ratio (N/S) and background to signal ratio (B/S):

- N/S ratio = standard deviation on 2300-2500 cm^{-1} / peak area on 908-988 cm^{-1} , $\nu_1 \text{PO}_4^{3-}$
- B/S ratio = peak area on 799-819 cm^{-1} , $\nu(\text{C-O-C})$ / peak area on 908-988 cm^{-1} , $\nu_1 \text{PO}_4^{3-}$

Additional masks were applied, when necessary, e.g., to mask out pixels of non-apatite phases or burned regions. These individual masks were added, multiplied with the processed hyperspectral dataset, and averaged to generate a mean spectrum. Peak area filters (plus peak width filters) were then applied to quantify the associated mineral and matrix species

(Table A.2). All measures were recorded and transported to JMP® (Version 15, SAS Institute Inc.) for statistical analysis.

Statistical analyses were conducted in JMP®. All data, including the size of calcifications (measured via the magic wand tool in ImageJ), integrated band areas, and clinical patient data, and micro-CT scoring, were transported and organized into one large JMP table. To compensate for the use of different laser power and allowing for direct comparison among calcifications of interest, the ratios of two band areas were calculated. Linear regression models were applied to explore any potential relationships between two parameters. A total of five parameters were then selected for hierarchical clustering analysis. A heat map of 84 calcifications of interest was generated using the "ward" method, labeled by the micro-CT scores, and two-way clustered. Two additional colormap columns - mineral form (single vs. aggregate) and patient gender - were added and a total of 5 clusters were adopted for the final configuration.

2.3 Results

Twenty-one excised aortic valves samples from 20 patients (M = 10, F = 6, N/D = 4) were provided by the Butcher group. Micro-CT was first performed on all 21 valve samples to visualize macrocalcifications and determine the level of calcifications for each sample (Figure A.1). A subgroup of 13 valve samples from 13 patients (M = 7, F = 5, N/D = 1) were selected, based on factors including continuous micro-CT scores, sample validity (e.g., no myocardial wall attached, clinical data), and budget, and proceeded with sample processing. Among the 13 valve samples, the 9 samples from 9 patients (M = 6, F = 2, N/D = 1) with relatively high micro-CT scores (score > 50) were embedded in PMMA and sectioned, while the other 4 samples from 4 patients (M = 1, F = 3) with low micro-CT scores (score < 50) were frozen in

OCT compound, followed with cryosection. Two serial sections were stained with von Kossa and Movat Pentachrome, to depict minerals and tissue architecture, and a third was reserved for Raman analysis. Unfortunately, since cryosectioning provided thick, segmented sections with high surface roughness that could barely be mapped under Raman, we focused mostly on the 9 PMMA-embedded samples. A total of 105 calcifications (103 calcifications from the 9 PMMA-embedded samples and 2 calcifications from cryosection) from 10 patients (M = 6, F = 3, N/D = 1) were mapped via Raman (Ch. 2.3.2).

For each Raman map, only the pixels with clear mineral signals were included and averaged to construct a mean Raman spectrum that represents the calcification of interest. A total of 90 mean Raman spectra from 8 patients (M = 5, F = 2, N/D = 1) was further averaged and plotted on top of the standard deviation (Figure 2.8). Among the 90 calcifications, 84 calcifications of interest from the same 8 patients were selected (6 calcifications were excluded due to negligible Amide III content) and hierarchically clustered to explore the relationships between mineral and matrix components (Ch. 2.3.3).

2.3.1 Micro-CT analysis

Micro-CT was first performed to characterize macrocalcifications of 21 valve samples from 20 patients (M = 10, F = 6, N/D = 4). The combination of gradient and transparency was used to construct three-dimensional models of calcified valve samples. Voxels with high CT numbers were colored in yellow, indicative of valvular calcifications, and those with low CT numbers in red for tissue matrix (Figure 2.1B). The level of calcification was then calculated by index sum scoring, a mathematical algorithm built upon volume and CT numbers (Figure 2.1C-G). The wide span of the scores, ranging from 0 (N = 5) to over 500, demonstrated the range of mineralization density in aortic valves at the time of surgery (Figure 2.1H). We found

that valves with low micro-CT scores (score < 200) tended to have clustered calcifications at the middle “theta” region, while those with high scores (score > 300) had calcifications that filled almost the entire space (Figure A.1). These results demonstrated that micro-CT could be used to differentiate the 3D spatial distribution of macro-calcifications and quantify the level of calcification, but the information collected was so limited that additional characterization tools were of necessity to advance the study of valvular calcifications.

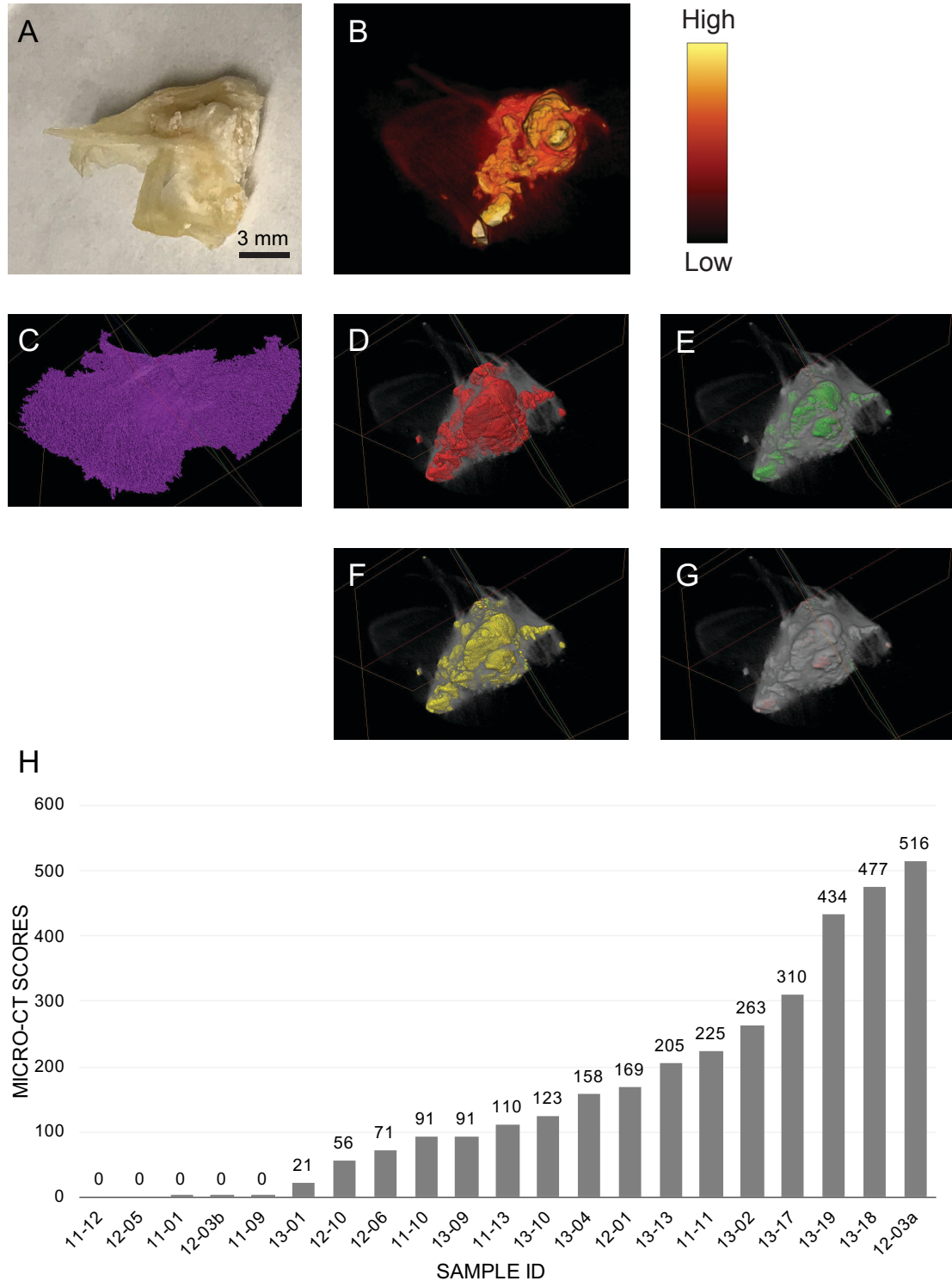


Figure 2. 1. Micro-CT modeling of a patient valve sample and index sum scoring. A). A macroscopic graph of a representative calcified human aortic valve sample. B). A micro-CT model of the same valve sample. Color gradient (yellow to red) and transparency are coupled to depict regions of calcifications. C-G). Voxels were assigned to five bins: tissue (purple, C), light calcification (red, D), medium calcification (green, E), heavy calcification (yellow, F), and extremely heavy calcification (pink, G). H).

The micro-CT scores of all 21 samples. The wide range of the scores demonstrated the range of mineralization density in aortic valves at the time of surgery.

2.3.2 Raman mapping of valvular calcifications

After characterizing macrocalcifications using micro-CT, we employed histological staining and Raman microscopy to investigate microcalcifications: the von Kossa stain was used as a guide to determine the regions of interest, and a confocal Raman microscope to characterize and map valvular calcifications (Figure A.3). A total of 105 maps were collected from 10 patient valves (M = 6, F = 3, N/D = 1). To combat the considerable variation in calcification size, ranging from 2 μm to over 200 μm in diameter, a size-based mapping strategy was developed to prioritize small- and medium-sized calcifications. For large calcifications with size over 2000 μm^2 , only the periphery regions where the minerals contacted matrix (and PMMA) were mapped. Raman mapping provided clear evidence of both mineral and matrix species. We found two types of valvular calcifications: carbonated hydroxyapatite (CHA) and whitlockite (WL). CHA was the dominant mineral species that could be traced everywhere in almost all sections of calcified valve samples (105/105 maps), while WL was a minor phase, rarely found, that appeared either at the periphery of or far away from large mineral deposits (4/105 maps). The size and shape of the two were also in two extremes. CHA was found in small, single deposits to large aggregates with size ranging from less than 100 μm^2 to more than 0.6 mm^2 and in a myriad of shapes, including but not limited to ellipsoids, diamonds, and rods. WL was often found as punctate and dispersed, with a maximum size less than 10 μm^2 .

Raman mapping also presented at least three dominant matrix components: collagen, elastin, and lipid. Since elastin shares spectral features with both collagen and general proteins (e.g., Amide III), unequivocally quantifying or even discriminating the

presence of elastin within mixed spectral regions was difficult and so we shifted the focus to lipid and collagen, due to their relative spectral isolation. Among the 105 Raman maps, 56 of them showed signals of lipid and 20 of them clear traces of collagen. *Moreover, we found that increasing calcification size was coupled with both decreasing lipid content and increasing collagen signals.*

We found that small calcifications, with size less than $500 \mu\text{m}^2$, tended to have high lipid content. The association was first observed in univariant Raman maps, where the pixels of the minerals ($\nu_1 \text{PO}_4^{3-}$) colocalized with those of the lipids (CH_2 twisting) (Figure 2.2A-L). However, since univariant maps were unable to fully discriminate one species from another within the filtered spectral regions, e.g., lipid and PMMA (as circled in Figure 2.2K&L), we thus proceeded to mean Raman spectra, averaged from pixels that contained clear mineral signals, to eliminate any interference from irrelevant species. The association between minerals and lipids was confirmed by mean Raman spectra. Figure 2.2M showed the mean Raman spectra of six small calcifications of interest with size ranging from $83\text{-}473 \mu\text{m}^2$ where minerals (i.e., CHA) associated strongly with lipids. Two Raman fingerprints of lipids, a peak at $\sim 1300 \text{ cm}^{-1}$ (CH_2 twisting) and a prominent shoulder at $\sim 2850 \text{ cm}^{-1}$ (symmetric CH stretching), were colored in yellow (Figure 2.2M).

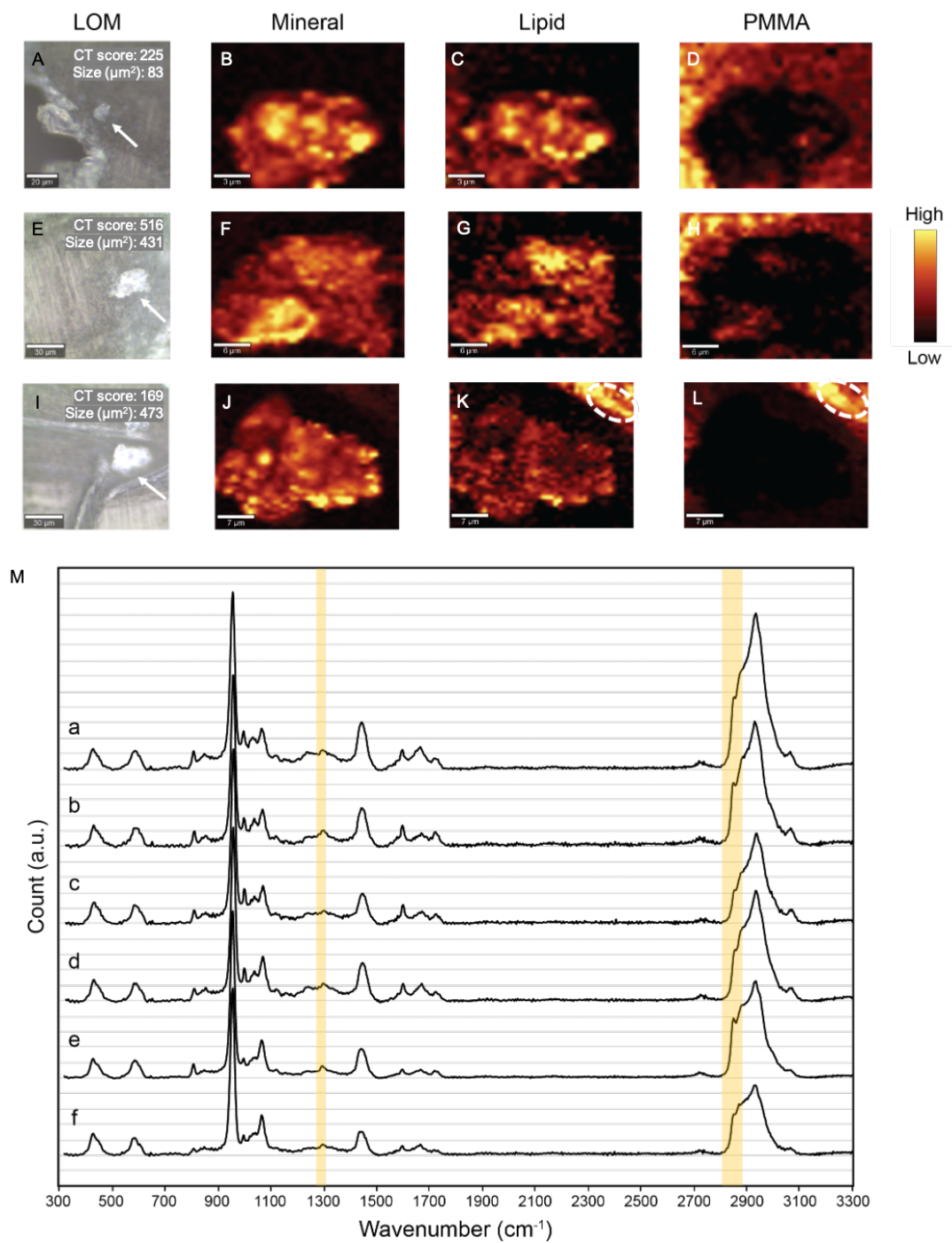


Figure 2. 2. Univariate Raman maps and mean Raman spectra show that minerals associate with lipids in small calcifications. A, E, I). Light optical microscope images of three small calcifications. B-D, F-H, J-L). Univariate Raman maps of the three calcifications. Peak areas filters of $\nu_1 \text{PO}_4^{3-}$, CH_2 twisting, and C-O-C stretching were used for constructing univariate Raman maps of mineral, lipid, and PMMA, accordingly. M). Six mean Raman spectra from six small calcifications with size ranging from 83-473 μm^2 show strong association between CHA and lipid. Two characteristic spectral regions of lipids are colored in yellow.

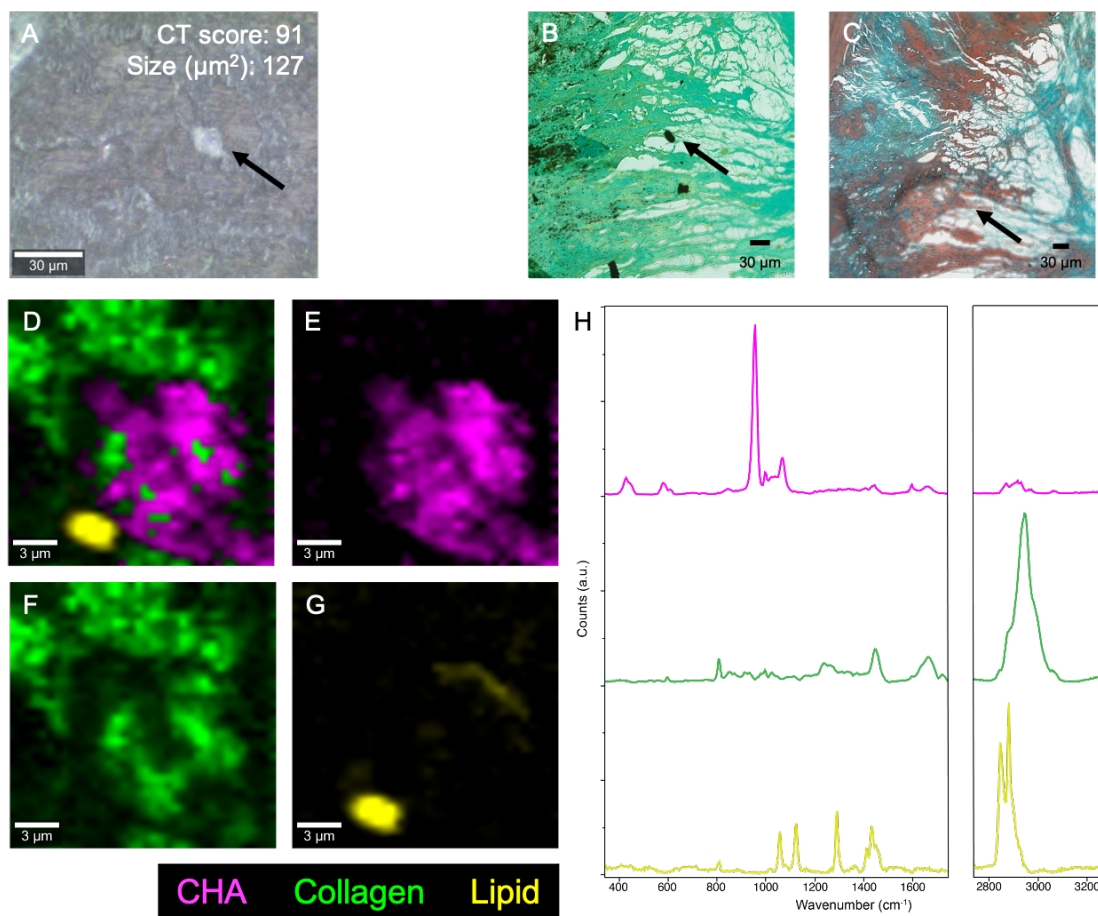


Figure 2. 3. An uncommon yet fascinating small calcification associated with lipid. A). Light optical image of the calcification of interest. B, C). Histological staining of the same calcification. von Kossa (B) showed the presence of the calcium phosphate and Movat Pentachrome (C) identified collagen as a major species of the surrounding matrix. D-G). Raman combinational maps showing CHA (magenta) and lipid (yellow) juxtaposed on collagen fibers (clover). H) The three bases Raman spectra for CHA, collagen, and lipid.

An uncommon yet fascinating small calcification was shown in Figure 2.3 from a female patient with a micro-CT score of 91. A small particle of calcium phosphate was seen in the von Kossa stain (Figure 2.3B) and its surrounding matrix was composed mainly of collagen fibers, as indicated by the Movat stain (Figure 2.3C). From Raman, the mineral phase was consistent with CHA. Combinational Raman maps showed a lipid droplet and collagen fibers being juxtaposed with the CHA (Figure 2.3D-G). The lipid droplet was consistent with a saturated fatty acid (Figure 2.3H, yellow), based to the presence of two intense peaks at

$\sim 1090\text{ cm}^{-1}$ (vibration of gauche conformation) and at $\sim 1130\text{ cm}^{-1}$ (C-C stretching), and the unique shape of a peak complex at $\sim 1430\text{ cm}^{-1}$ (CH_2 bending)⁹.

We also found that large calcifications, with size larger than $2000\text{ }\mu\text{m}^2$, associated more closely with collagen. Colocalization of mineral ($\nu_1\text{ PO}_4^{3-}$) and collagen (Amide III) pixels was observed in univariant Raman maps (Figure 2.4A-L). To combat the interference of collagen and PMMA within the same univariant Raman maps (circled in Figure 2.4G,H,K,L), mean Raman spectra were explored. The association between minerals and collagen was confirmed by mean Raman spectra. Figure 2.4M displayed five representative mean spectra that contained both mineral (i.e., CHA) and collagen signals. Two characteristic Raman peaks of collagen, a peak complex at $\sim 875\text{ cm}^{-1}$ (Pro/Hyp) and Amide III, were colored in green (Figure 2.4M).

A characteristic large calcification was shown in Figure 2.5 (also in Figure 2.4A-D) from a male patient with a micro-CT score of 434. The von Kossa stain determined the approximate location of the calcification (Figure 2.5B), while the Movat stain identified its surrounding matrix as highly dense, yet poorly organized collagen fibers (Figure 2.5C). From Raman, the mineral phase was consistent with CHA. Combinational Raman maps displayed CHA situated among collagen fibers: more collagen signals were detected at the periphery than the center of the calcification (Figure 2.3D-F).

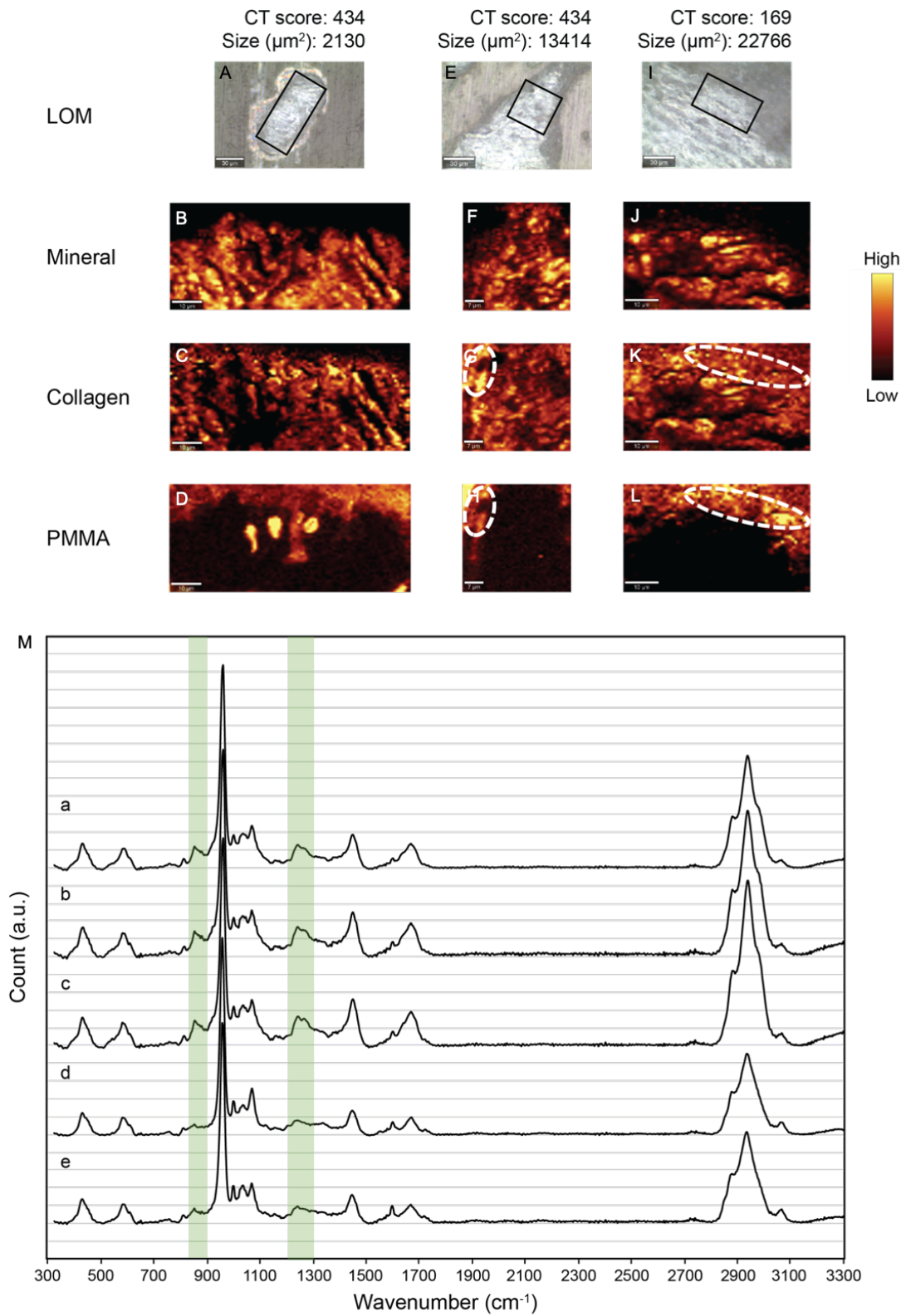


Figure 2. 4. Univariate Raman maps and mean Raman spectra show that minerals associate with collagen in large calcifications. A, E, I). Light optical microscope images of the periphery of three large

calcifications. B-D, F-H, J-L). Univariate Raman maps of the three calcifications. Peak areas filters of ν_1 PO_4^{3-} , Amide III, and C-O-C stretching were used for constructing univariate Raman maps of mineral, collagen, and PMMA, accordingly. M). Five mean Raman spectra from five medium to large calcifications with size ranging from 1679-22766 μm^2 show strong association between CHA and collagen. Two characteristic spectral regions of collagen are colored in green.

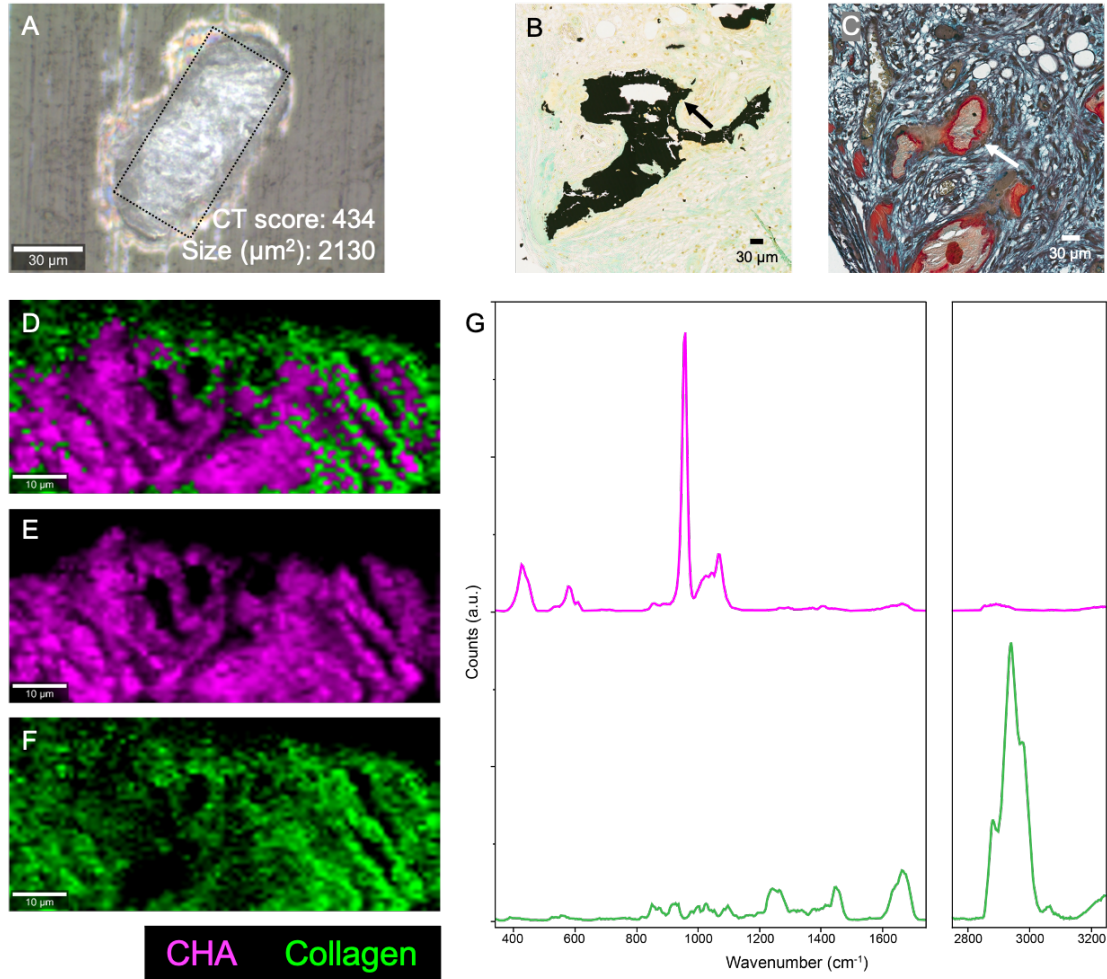


Figure 2. 5. A large calcification bounded by collagen fibers. A). Light optical image of the calcification of interest. B, C). Histological staining of the same calcification: von Kossa (B) showed the presence of the calcium phosphate and Movat Pentachrome (C) identified the surrounding matrix as highly dense yet poorly organized collagen fibers. D-G). Raman combinational maps showing CHA (magenta) situated among collagen fibers (clover). H) The two bases Raman spectra for CHA and collagen.

A bar chart was used to summarize and extrapolate potential trends between calcification size and the association of mineral and matrix species (Figure 2.6). The rate of occurrence for CHA associated with lipids decreased about a third from 68% to 43% when the calcification size increased from small calcifications (n = 34), with size less than 500 μm^2 ,

to large calcifications ($n = 28$), with size more than $2000 \mu\text{m}^2$. Such a trend is inverted for collagen. The rate of occurrence for CHA associated with collagen almost doubled from 15% to 29% when the calcification size increased from small to large calcifications. Medium calcifications ($n = 41$), with size ranged from 500 to $2000 \mu\text{m}^2$, showed combined traits of the other two groups.

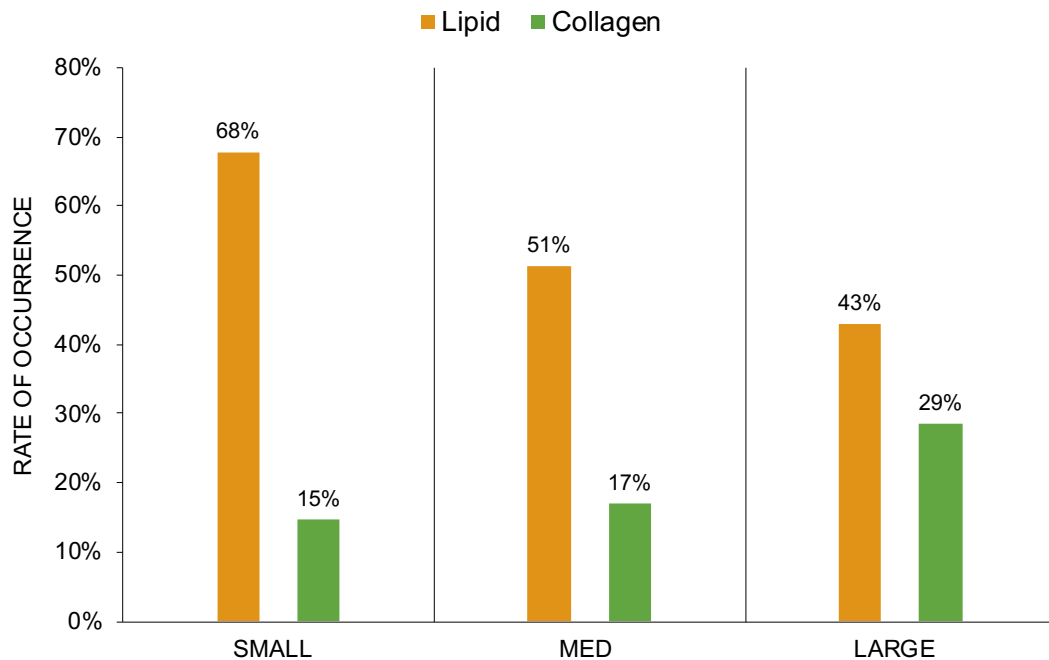


Figure 2. 6. Raman univariant mapping reveals the correlation between calcification size and matrix species. Small calcifications ($n = 34$), with size less than $500 \mu\text{m}^2$, are intimately associated with lipids, and less with collagen. On the contrary, large calcifications ($n = 28$), with size large than $2000 \mu\text{m}^2$, are more associated with collagen fibers, and less with lipids. Medium calcifications ($n = 41$), with size ranged from 500 to $2000 \mu\text{m}^2$, show combined traits of the other two groups.

Last, we discovered a whitlockite cluster at the edge of a tissue section, away from the calcification nodule, from a female patient with a micro-CT score of 21 (Figure A.2). These whitlockite particles could barely be recognized in the von Kossa stain (Figure 2.7B) and were surrounded by a seemingly normal, healthy matrix that contained collagen fibers, according to the Movat stain (Figure 2.7C). From Raman, the mineral phase was identified as

whitlockite, based on the peak shift of both ν_1 and ν_2 PO_4^{3-} and the unique peak shape of ν_4 PO_4^{3-} (Figure 2.7H, magenta). Combinational Raman maps showed that whitlockite particles clustered in a matrix full of collagen and lipid species. According to the associated Raman spectra, the unique peak at 700 cm^{-1} (carbon backbone vibration mode), in combination with the peak at 1740 cm^{-1} (C=O stretching mode), affirmed the lipid species as cholesterol ester (Figure 2.7H, yellow). There were also tiny hydroxyapatite particles at the vicinity not captured by the NMF and were thus not shown on the combinational Raman maps.

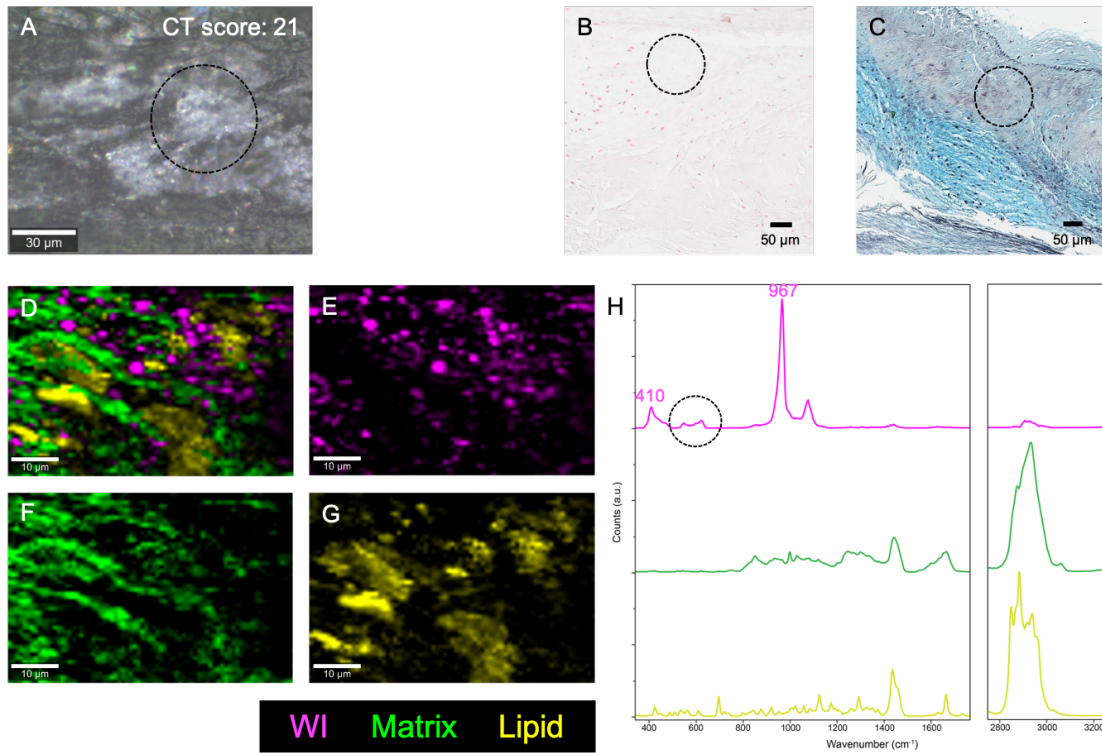


Figure 2. 7. A rarely found whitlockite cluster surrounded by collagen fibers and lipid species. A). Light optical image of the calcification cluster. B, C). Histological staining of the same calcification cluster: von Kossa shows negligible signals of calcification (B) and Movat Pentachrome (C). D-G). Raman combinational map showing whitlockite (magenta), collagen fibers (green), and cholesterol (yellow). H) The three bases Raman spectra for CHA, collagen, and cholesterol.

2.3.3 Analysis of mean Raman spectra and hierarchical clustering

The mean Raman spectra from a group of selected hyperspectral datasets ($n = 90$) were further explored. A mean spectrum of these 90 averaged spectra was plotted on top of the standard deviation to reflect the variations of mineral-matrix species present among the 90 calcifications of interest (Figure 2.8). There were relatively minimal variations among the mineral signals (e.g., $\nu_{2,4} \text{PO}_4^{3-}$ and $\nu_1 \text{CO}_3^{2-}$). The slight variation of the $\nu_1 \text{PO}_4^{3-}$ peak was likely a result from peak shifting. Two peaks at $\sim 809 \text{ cm}^{-1}$ and $\sim 1726 \text{ cm}^{-1}$ could be attributed to PMMA, a spectral feature that could not be avoided throughout analysis. Most peak variations came from matrix species: Amide III (collagen and NCPs), the CH_2/CH_3 bending mode at $\sim 1445 \text{ cm}^{-1}$ (lipid, also protein), Amide I (protein), and the C-H complex (lipid and protein).

Raman peak areas and the peak width of $\nu_1 \text{PO}_4^{3-}$ were then calculated and mineral and matrix metrics were devised to assess mineral properties and quantify relative contributions of the underlying organic species. Because a precedence of clinically relevant Raman-based mineral and matrix properties has been established in bone⁵², where the mineral component consists of biogenic apatite, we chose similar metrics to describe the mineral and matrix in valvular calcification. We also examined lipid to protein ratio due to the importance of lipid involvement in disease progression. Five metrics: two for mineral (i.e., carbonate content and mineral crystallinity), two for colocalized matrix (i.e., lipid to protein ratio and collagen content), and one for both (i.e., mineral to matrix ratio) were further explored:

- Carbonate content = $\nu_1 \text{CO}_3^{2-} / \nu_1 \text{PO}_4^{3-}$
- Mineral crystallinity = $1 / \nu_1 \text{PO}_4^{3-}$
- Mineral to matrix ratio = $\nu_2 \text{PO}_4^{3-} / \text{Amide III}$

- Lipid to protein ratio = 2796-2860 cm^{-1} (lipid shoulder) / 2908-2930 cm^{-1} (NCPs)
- Collagen content = 1216-1284 cm^{-1} (collagen Amide III) / Amide III

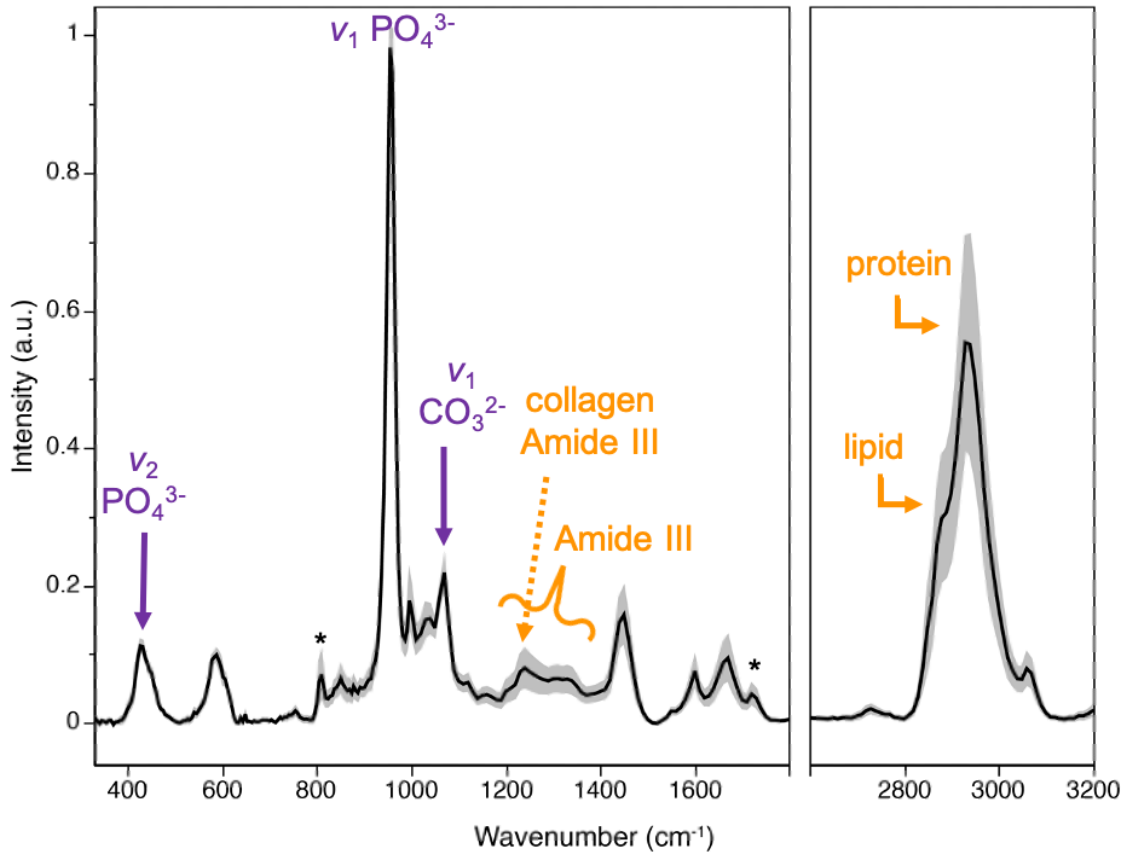


Figure 2. 8. The mean spectrum of 90 mean Raman spectra. A mean spectrum of 90 averaged mean Raman spectra was plotted on top of the standard deviation to reflect the variations of mineral-matrix species present among the 90 calcifications of interest.

A hierarchical clustering was performed on 84 calcifications from 8 patients (M = 5, F = 2, N/D = 1; 6 calcifications were excluded due to negligible Amide III content) via the five mineral-matrix metrics. Two other binary metrics, i.e., patient gender (male vs. female) and mineral form (single vs. aggregate), were added, along with the micro-CT scores, to establish the context for the 84 calcifications (Figure 2.10). There was a huge difference between the number of calcifications from male (n = 57) and from female (n = 18). The other 9 calcifications belonged to a patient with missing clinical data and were thus colored in white.

Figure 2.9 showed a comparison between single and aggregate calcifications: single calcifications ($n = 43$) were often found as solid blocks with defined boundary, while aggregate calcifications ($n = 41$) tended to have blurry boundaries and were composed of multiple dispersed subunits. Micro-CT scores were incorporated into the hierarchical clustering to both infer the disease state/severity and assign calcifications to patients. A total of five clusters were selected and color-coded as the final configuration (Figure 2.10).

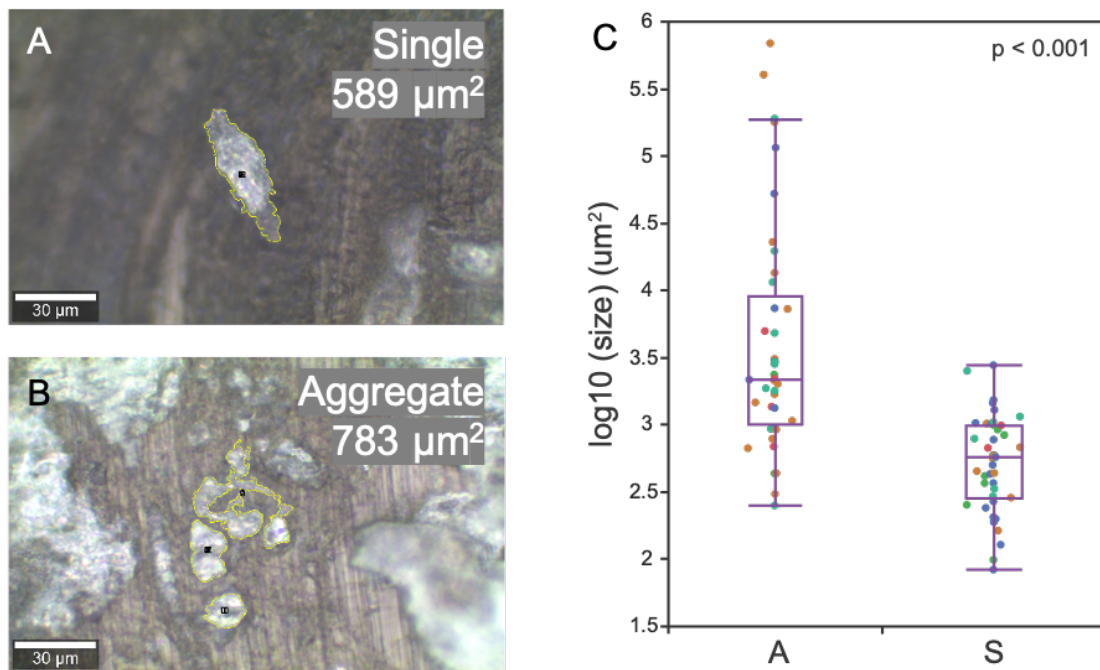


Figure 2. 9. Examples of single vs. aggregate calcifications and the correlation between mineral form and calcification size. A, B). light optical microscope images of representative small (A) and aggregate (B) calcifications with similar calcification size. C). A box plot shows that the mean size of aggregate calcifications ($n = 41$) is much larger than that of single calcifications ($n = 43$). The color of dots is consistent with the 5 hierarchical clusters.

Again, we found that lipid and collagen had an inverse relationship. Calcifications with high lipid content (cluster 1, 2, and the bottom subcluster of 3) exhibited the lowest collagen signals, and vice versa – the ones with high collagen signals (cluster 4, 5) coincided with the lowest lipid content. Interestingly, the former contained mostly single calcifications (lavender) while the later mainly aggregate calcifications (violet) (Figure 2.10). To further

explore the relationship, linear regression was applied to fit a scatter plot of lipid to protein ratio versus collagen to matrix ratio (Figure 2.11A). Though the data contains high variation ($R^2 = 0.375$), an inverse relationship between the two parameters is clear ($p < 0.001$).

We also found that valvular calcifications from female patients tended to have a higher crystallinity. The female calcifications (sky blue) in both cluster 3 and 4 had high mineral crystallinity, while the male calcifications (ocean blue) could have both high (cluster 3) and low mineral crystallinity (cluster 2, the top portion of cluster 4, and **cluster 5**) (Figure 2.10). A following box plot further confirmed that the mineral crystallinity of valvular calcifications was indeed higher in female patients than in male patients (Figure 2.11B).

Patients introduced another layer of complexity. Based on the distribution of calcifications within the 5 hierarchical clusters, we summarized two types of patients (Figure A.5). Type A patients ($N = 3$) had calcifications spread across 4 out of 5 clusters, while Type B patients ($N = 4$) had most calcifications concentrated within one cluster (one patient was excluded due to the low number of calcifications being included into the hierarchical clustering) (Table A.1). We have not detected any correlation between either micro-CT scores (indication of disease severity) and mineral-matrix fingerprints or micro-CT scores and patient heterogeneity.

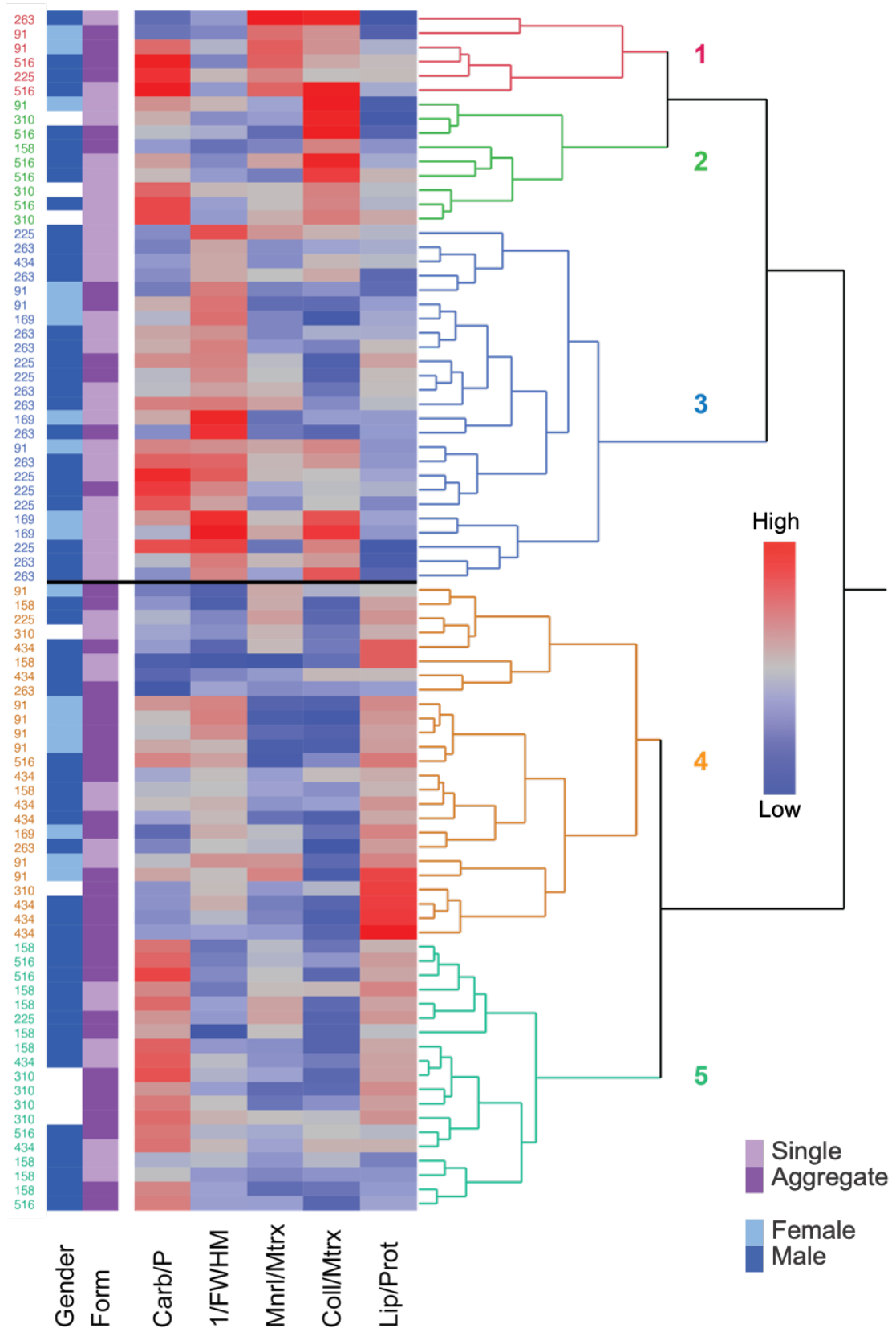


Figure 2. 10. Hierarchical clustering of calcifications using 5 mineral-matrix metrics from Raman. The rows represent the fingerprints of calcifications ($n = 84$ from 8 patients), while the columns correspond to metrics (5 mineral-matrix metrics, with gender and mineral form). Micro-CT scores are shown on the left and colored based on the 5 clusters.

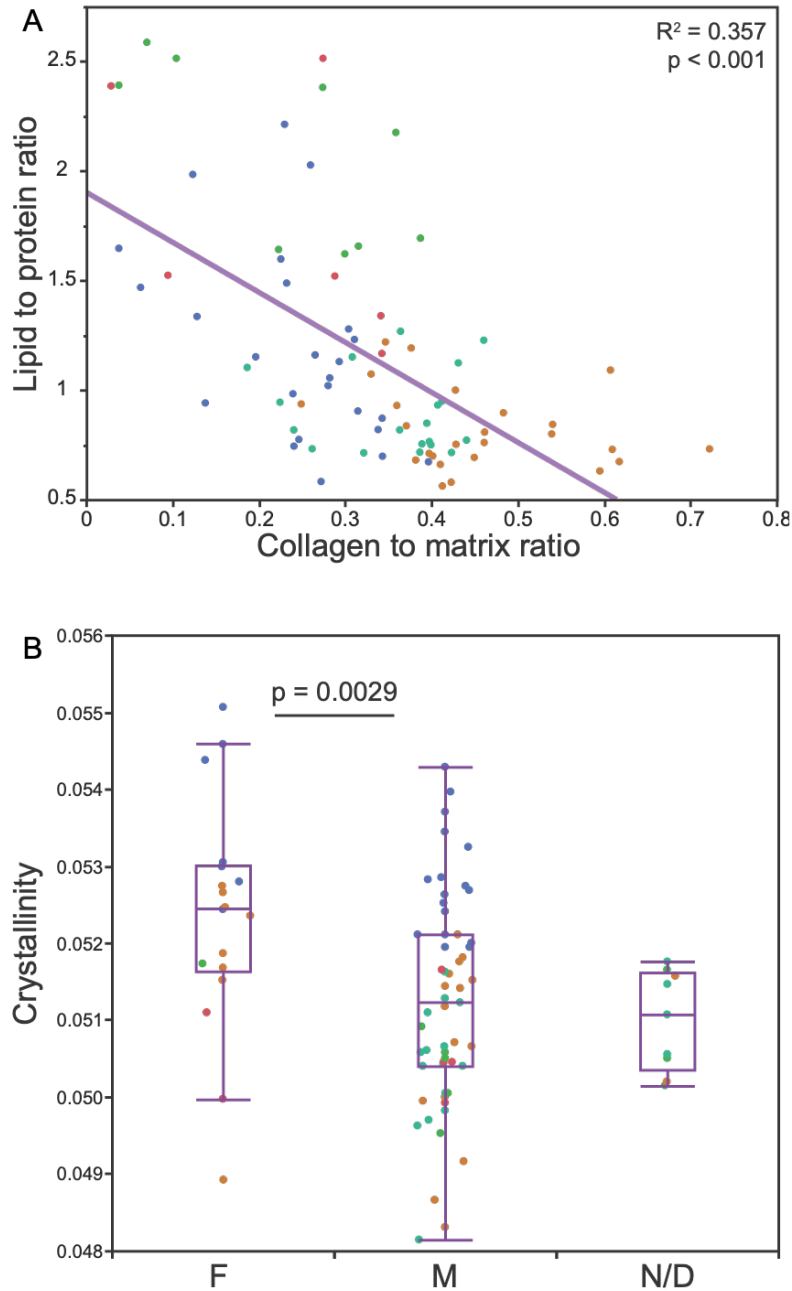


Figure 2. 11. Lipid vs. collagen content and crystallinity vs. gender. A). Linear regression is used to fit a scatter plot of lipid to protein ratio vs. collagen to matrix ratio. Though the data has high variation ($R^2 = 0.357$), an inverse relationship between the two parameters is clear ($p < 0.001$). B). A box plot of crystallinity vs. gender shows that the mean crystallinity of calcifications from female patients is higher than that of male patients ($p < 0.003$). The color of dots is consistent with the 5 hierarchical clusters.

2.4 Discussion

The results of this thesis lay the groundwork for incorporating Raman microscopy into the study of CAVD pathogenesis. Contrary to the traditional top-down methodology, we have employed a bottom-up approach to explore the underlying mineral-matrix relationships of valvular calcifications from a molecular/biochemical perspective. By studying both the mineral and the matrix compositions we believe we can learn about pathways by which the minerals form. These pathways can in turn give us insights into the cellular role(s) in calcification and the disease progression.

We have found two major types of valvular calcification intimately associated with the organic matrix: 1) single, small calcifications associated with lipid, and 2) large, aggregate calcifications associated with collagen. These two types are reminiscent of the mainstream theory of valvular calcifications: dystrophic calcification (i.e., the release of high concentration of calcium and phosphate associated with dead cell debris¹⁰) and heterotopic ossification (i.e., bone formation at the wrong place¹⁰). Small, lipid-rich calcifications seem to be a potential outcome of dystrophic calcification, and the combination of collagen and minerals does share some characteristics of bone formation. However, the Raman maps collected in this study can only provide snapshots of valvular calcifications when the diseased valves were extracted. These snapshots can only be used to support but unable to justify the underlying mechanisms. Whether the two types of calcifications belong to two stages of the same mineralization pathway or follow two separate pathways requires further investigation.

Extensive attention has been paid to the relationship between carbonate content and mineral crystallinity. In physiological mineralization (e.g., bone growth), carbonate ions are incorporated into the lattice of hydroxyapatite to form larger and more stoichiometric crystals, yielding a positive relationship between carbonate content and mineral

crystallinity¹¹. The inverted trend is found in both synthetic bone systems¹² and pathological mineralization, as recorded in both *Jennie Kunitake's* heat map on microcalcifications of breast cancer¹³ and a previous study on valvular calcification¹⁴. However, not only is linear regression unable to fit our data (Figure A.4A), but the hierarchical clustering heat map shows seemingly context-dependent results: the two metrics adopt a positive relationship in cluster 3 and 4, but exhibit a negative relationship in cluster 1, 2, and 5 (Figure 2.10). After fitting (Lorentzian) the ν_1 PO₄³⁻ peak and subtracting PMMA manually, we immediately find that carbonate content and mineral crystallinity (inverse of FWHM) adopt a positive relationship in the processed data ($R^2 = 0.612$, p-value < 0.0001), resembling that of physiological mineralization (Figure A.4B). Despite considerable effort, we are unable to grasp the rationale behind such data processing, and we thus decide to stay with the original numbers (Figure A.4A). We believe that the lack of correlation between carbonate content and mineral crystallinity has multiple causes: 1) mathematical difficulty of subtracting the underlying matrix bands beneath ν_1 PO₄³⁻, 2) the presence of additional, undetectable mineral phases, and 3) the combination of both physiological- and pathological-like calcification in valvular calcification.

We have also found that female calcifications exhibit higher mineral crystallinity, confirmed by the FWHM of ν_1 PO₄³⁻ peak, where a shorter FWHM corresponds to a higher mineral crystallinity (Figure 2.11B). However, *Gourgas et al.* suggests that female patients tend to have more non-apatitic phases, which, if incorporated with CHA, would inevitably widen the FWHM of ν_1 PO₄³⁻ peak, and thus contradict with our results¹⁵. A higher spectral resolution (i.e., ~ 0.5 cm⁻¹) by shifting the diffraction gratings might gain additional information regarding mineral phase. Clinically, female patients with less calcifications are found to have the same level of disease severity (e.g., peak aortic jet velocity, mean

transvalvular gradient) when compared to their male cohort¹⁶. Our results propose that a higher mineral crystallinity might be a possible explanation. Raman can indeed be applied to investigate how mineral properties vary as a result of gender difference. However, beware that the correlation was drawn from a comparison between 2 female patients (16 calcifications) and 5 male patients (54 calcifications). More calcifications from more patients, especially female patients, are necessary to further explore the gender mystery.

REFERENCES

1. Kostyunin AE, Yuzhalin AE, Ovcharenko EA, Kutikhin AG. Development of calcific aortic valve disease: Do we know enough for new clinical trials? *Journal of Molecular and Cellular Cardiology*. 2019;132(May):189-209. doi:10.1016/j.yjmcc.2019.05.016
2. Driscoll K, Cruz AD, Butcher JT. Inflammatory and Biomechanical Drivers of Endothelial-Interstitial Interactions in Calcific Aortic Valve Disease. *Circulation Research*. Published online 2021:1344-1370. doi:10.1161/CIRCRESAHA.121.318011
3. Yutzey KE, Demer LL, Body SC, et al. Calcific aortic valve disease: A consensus summary from the alliance of investigators on calcific aortic valve disease. *Arteriosclerosis, Thrombosis, and Vascular Biology*. 2014;34(11):2387-2393. doi:10.1161/ATVBAHA.114.302523
4. Richards, J.M. (2015). Endothelial regulation of valve interstitial cells in calcific aortic valve disease. [Doctoral dissertation, Cornell University, Ithaca]. doi:10.1145/3132847.3132886
5. Gee, T.W. (2020) Coregulatory mechanisms of cellular recruitment in fibrocalcific aortic valve disease [Doctoral dissertation, Cornell University, Ithaca].
6. Mangialardo S, Cottignoli V, Cavarretta E, Salvador L, Postorino P, Maras A. Pathological biominerals: Raman and infrared studies of bioapatite deposits in human heart valves. *Applied Spectroscopy*. 2012;66(10):1121-1127.
7. Prieto RM. Study on the structure and composition of aortic valve calcific deposits. etiological aspects. *Journal of Biophysical Chemistry*. 2011;02(01):19-25. doi:10.4236/jbpc.2011.21003
8. Pilarczyk M, Czamara K, Baranska M, et al. Calcification of aortic human valves studied in situ by Raman microimaging: Following mineralization from small grains to big deposits. *Journal of Raman Spectroscopy*. 2013;44(9):1222-1229. doi:10.1002/jrs.4352
9. Czamara K, Majzner K, Pacia MZ, Kochan K, Kaczor A, Baranska M. Raman spectroscopy of lipids: a review. *Journal of Raman Spectroscopy*. 2015;46(1):4-20. doi:10.1002/jrs.4607
10. Vidavsky N, Kunitake JAMR, Estroff LA. Multiple Pathways for Pathological

Calcification in the Human Body. *Advanced Healthcare Materials*. Published online December 4, 2020:2001271. doi:10.1002/adhm.202001271

11. Taylor EA, Donnelly E. Raman and Fourier transform infrared imaging for characterization of bone material properties. *Bone*. 2020;139(May). doi:10.1016/j.bone.2020.115490
12. Taylor EA, Mileti CJ, Ganesan S, Kim JH, Donnelly E. Measures of Bone Mineral Carbonate Content and Mineral Maturity/Crystallinity for FT-IR and Raman Spectroscopic Imaging Differentially Relate to Physical–Chemical Properties of Carbonate-Substituted Hydroxyapatite. *Calcified Tissue International*. 2021;109(1):77-91. doi:10.1007/s00223-021-00825-4
13. Kunitake, J. A. M. R. (2021). Correlative imaging of benign and cancerous breast calcifications: implications for prognosis and insights into lipid dysregulation. [Doctoral dissertation, Cornell University, Ithaca].
14. Richards JM, Kunitake JAMR, Hunt HB, et al. Crystallinity of hydroxyapatite drives myofibroblastic activation and calcification in aortic valves. *Acta Biomaterialia*. 2018;71:24-36. doi:10.1016/j.actbio.2018.02.024
15. Gourgas O, Khan K, Schwertani A, Cerruti M. Differences in mineral composition and morphology between men and women in aortic valve calcification. *Acta Biomaterialia*. 2020;106:342-350. doi:10.1016/j.actbio.2020.02.030
16. Aggarwal SR, Clavel MA, Messika-Zeitoun D, et al. Sex differences in aortic valve calcification measured by multidetector computed tomography in aortic stenosis. *Circulation: Cardiovascular Imaging*. 2013;6(1):40-47. doi:10.1161/CIRCIMAGING.112.980052

CHAPTER 3

CONCLUSION & FUTURE DIRECTIONS

The overarching goal of this study is to understand the pathogenesis and biogenic formation during the progression of calcific aortic valve disease. Much research has focused on cell signaling pathways and maladaptive remodeling of the valvular matrix. Little is known, however, about the pathological mineralization process from a material science perspective. In this study, Raman microscopy was employed in combination with micro-CT and histology to characterize mineral and organic matrix properties in the context of pathology. Carbonated hydroxyapatite was found to be the predominant phase of valvular calcification, though traces of whitlockite and octacalcium phosphate were also detected. We found that the mineral crystallinity of valvular calcification was higher for female than male patients. Though calcifications were extremely heterogeneous across and among patients in terms of mineral size, micro-CT scoring, matrix composition, etc., small calcifications tended to associate strongly with lipids, while large calcifications with collagen. The association of specific matrix species with calcifications size could reflect different events in the pathological progression of the disease (e.g., inflammation and fibrosis), and warranted further investigation.

If collecting over 100 Raman maps (not including massive overruns) has taught me one lesson about acquiring high-quality Raman spectra, that lesson will be on surface roughness. Theoretically, Raman can map all regions on a sample surface. In practice, however, the threshold of “true surface” feature is rather limited and having a section with *smooth* surface is truly the key to yield strong Raman signals and reduce unnecessary compromises. Although we have not found traces of valvular cells, *Jennie Kunitake's* previous

work has substantiated that Raman can indeed detect signals of both cell DNA and cytochrome *c*¹. Several adjustments to the existing workflow are worth exploring. First, cryosection should be considered before PMMA embedding, due to its short turnover rate (cryosection: half a day; PMMA: a month) and less chemicals being introduced to embed tissues. Second, the diffraction gratings of the spectrometer can be shifted from 300 l/mm to 1200 l/mm, which will elevate the spectral resolution from $\sim 3 \text{ cm}^{-1}$ to $\sim 0.5 \text{ cm}^{-1}$, at the cost of losing the C-H complex, but with the potential to gain additional information regarding mineral phase. Third, sample sections can be submerged in solution, coupled with the 785 cm^{-1} laser excitation source and a much higher laser power to reduce/eliminate fluorescence, without sacrificing the intensity of the Raman signals.

Since vibrational spectroscopy excels at differentiating inorganic minerals from organic matrix, it is a technique so perfect that is almost customized for studying fibrocalcific remodeling of valvular ECM. Besides Raman microscopy, Fourier transform infrared spectroscopy (FTIR) can be incorporated into the workflow to complement Raman. A recent review paper by *Taylor & Donnelly* provides a thorough comparison between these two techniques³. An ideal workflow will be to scan the whole valvular section via FTIR first and then delve into the small regions of interest via Raman. Meanwhile, other characterization modalities can be employed to assist vibrational spectroscopy: scanning electron microscopy (SEM) can provide morphogenic and topographic information of sample surface, and energy dispersive x-ray spectroscopy (EDS) can yield elemental analysis⁴. Several future directions include but are not limited to 1) incorporating SEM/EDS into the workflow to further examine the heterogeneity of valvular calcification; 2) mimicking dystrophic calcification (e.g., pumping high concentration of Ca^{2+} and PO_4^{3-} ions into a medium of dead VIC debris and cholesterol) to study mineral growth; and 3) applying mineral-matrix metrics into *in vivo*

murine studies to inspect the impact of gender difference on valvular calcification. I sincerely hope that with the assistance of these characterization techniques, my successors can further explore the biomineralization pathways of valvular calcification and develop some metric applicable to the diagnosis (or even prognosis) of calcific aortic valve disease.

REFERENCES

1. Vidavsky N, Kunitake JAMR, Diaz-Rubio ME, et al. Mapping and Profiling Lipid Distribution in a 3D Model of Breast Cancer Progression. *ACS Central Science*. 2019;5(5):768-780. doi:10.1021/acscentsci.8b00932
2. Olsson M, Thyberg J, Nilsson J. Presence of oxidized low density lipoprotein in nonrheumatic stenotic aortic valves. *Arteriosclerosis, Thrombosis, and Vascular Biology*. 1999;19(5):1218-1222. doi:10.1161/01.ATV.19.5.1218
3. Taylor EA, Donnelly E. Raman and Fourier transform infrared imaging for characterization of bone material properties. *Bone*. 2020;139(May). doi:10.1016/j.bone.2020.115490
4. Kunitake JAMR, Choi S, Nguyen KX, et al. Correlative imaging reveals physiochemical heterogeneity of microcalcifications in human breast carcinomas. *Journal of Structural Biology*. 2018;202(1):25-34. doi:10.1016/j.jsb.2017.12.002

APPENDIX

A.1 Graphs of Calcified Valve Samples

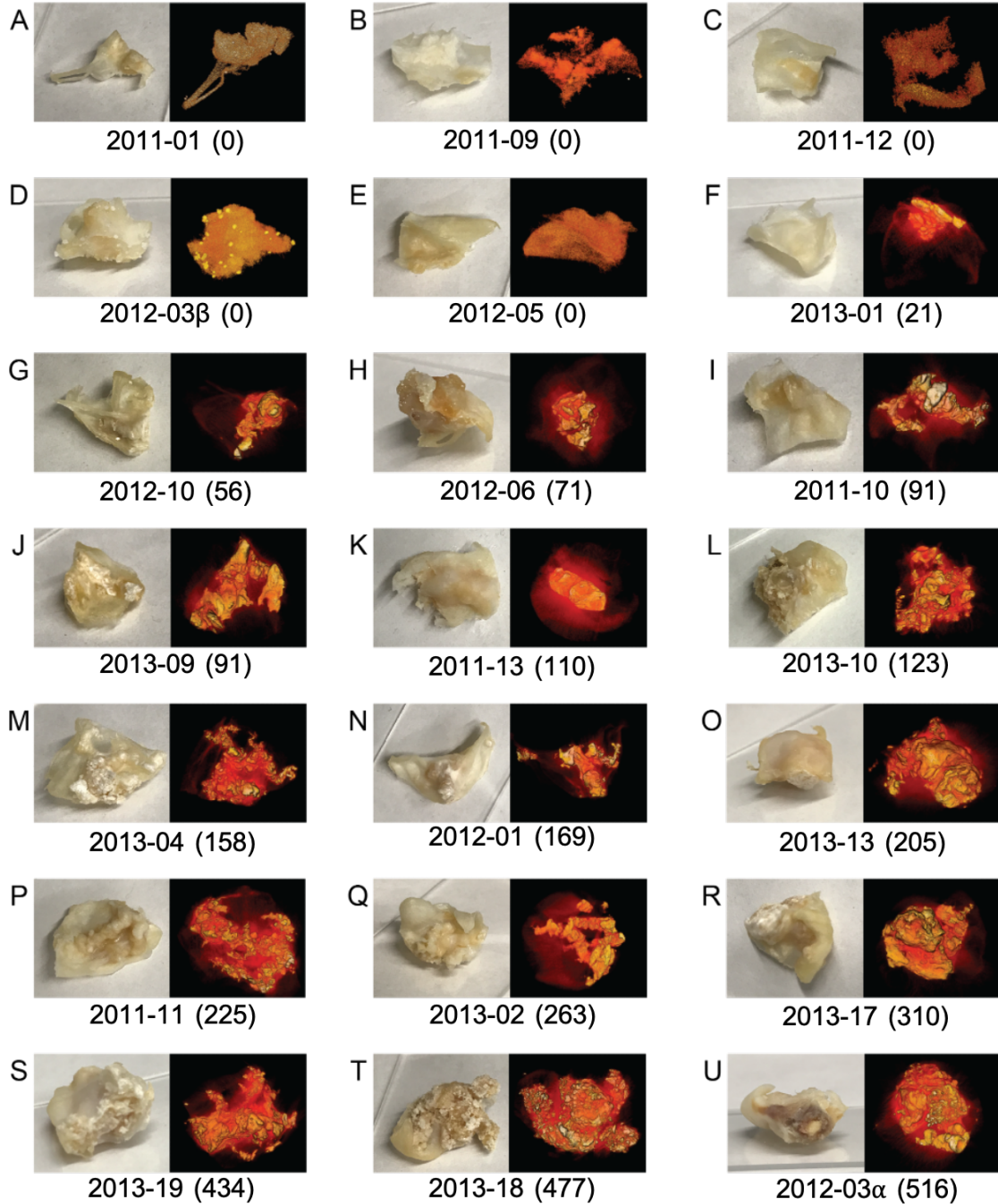


Figure A. 1. Macroscopic graphs and micro-CT models of all 21 calcified aortic valve samples. A-U). 21 pairs of macroscopic graphs (left) and micro-CT models (right), along with the sample ID and the micro-CT scores (in bracket). The sample ID and micro-CT scores correspond to the ones in Figure 2.1.H.

A.2 Aortic Valve Sample Sections

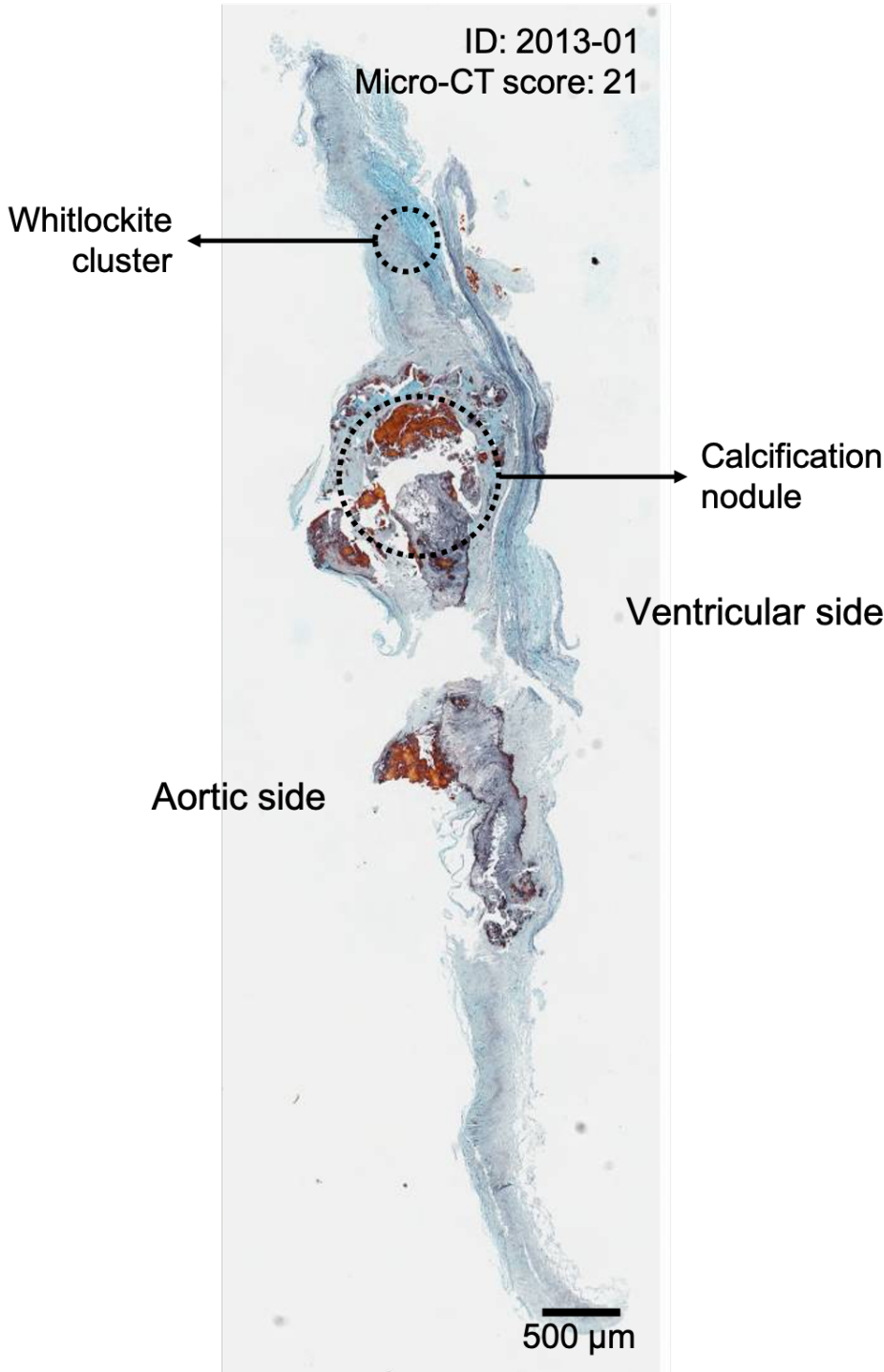


Figure A. 2. Movat Pentachrome stain of a valve section from a female patient with a micro-CT score of 21. Two regions, calcification nodule and whitlockite cluster, are circled. Both aortic and ventricular side of the valve leaflet are labeled. The region of whitlockite cluster is mapped via Raman (Figure 2.7).

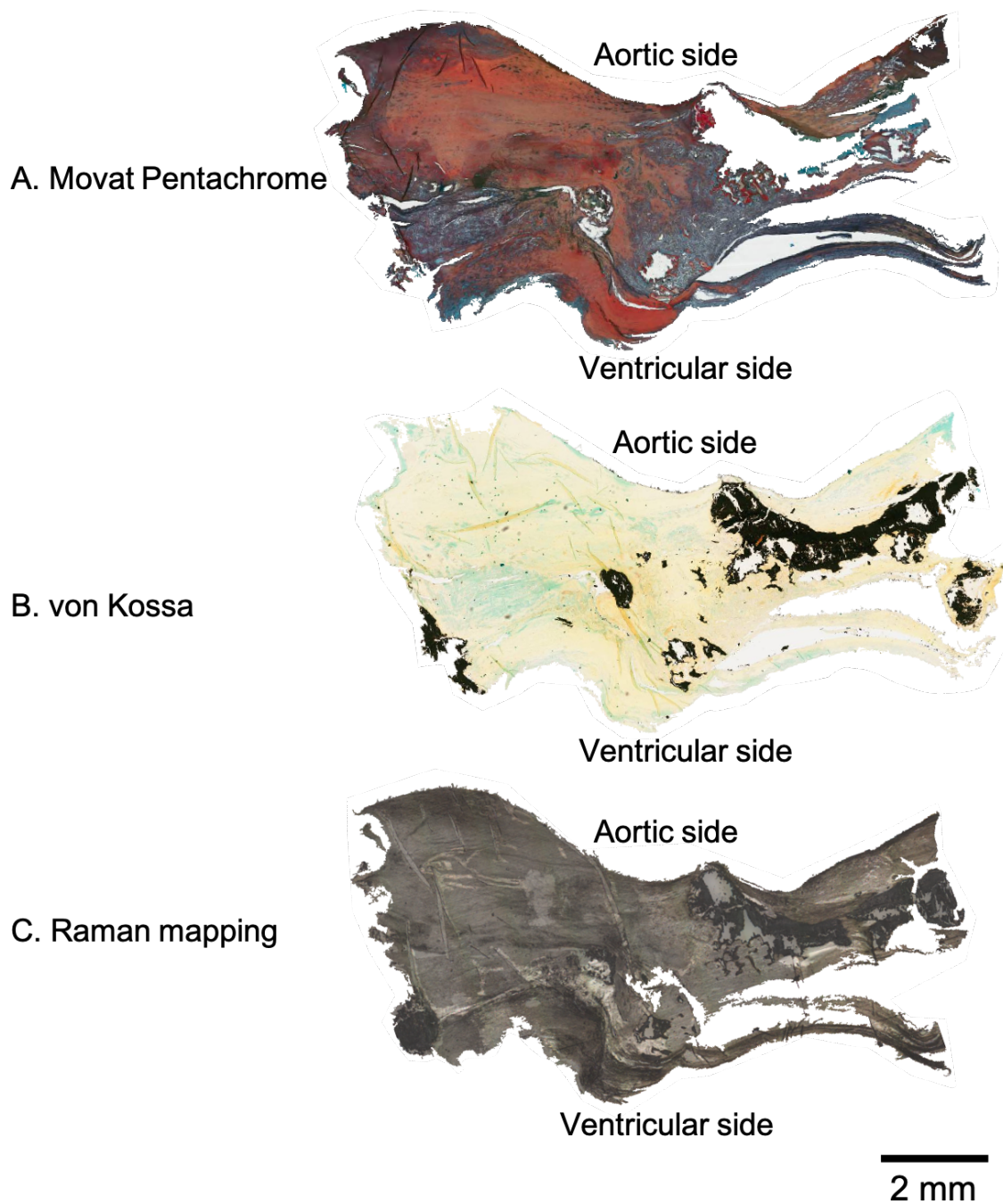


Figure A. 3. Three serial sections from a patient with a micro-CT score of 434. A). Movat Pentachrome stain is used to study the tissue architecture. **B).** von Kossa stain is employed as a guide to determine the regions of interest. **C).** Raman mapping is performed to explore the mineral-matrix relationships.

A.3 Carbonate Content vs. Crystallinity

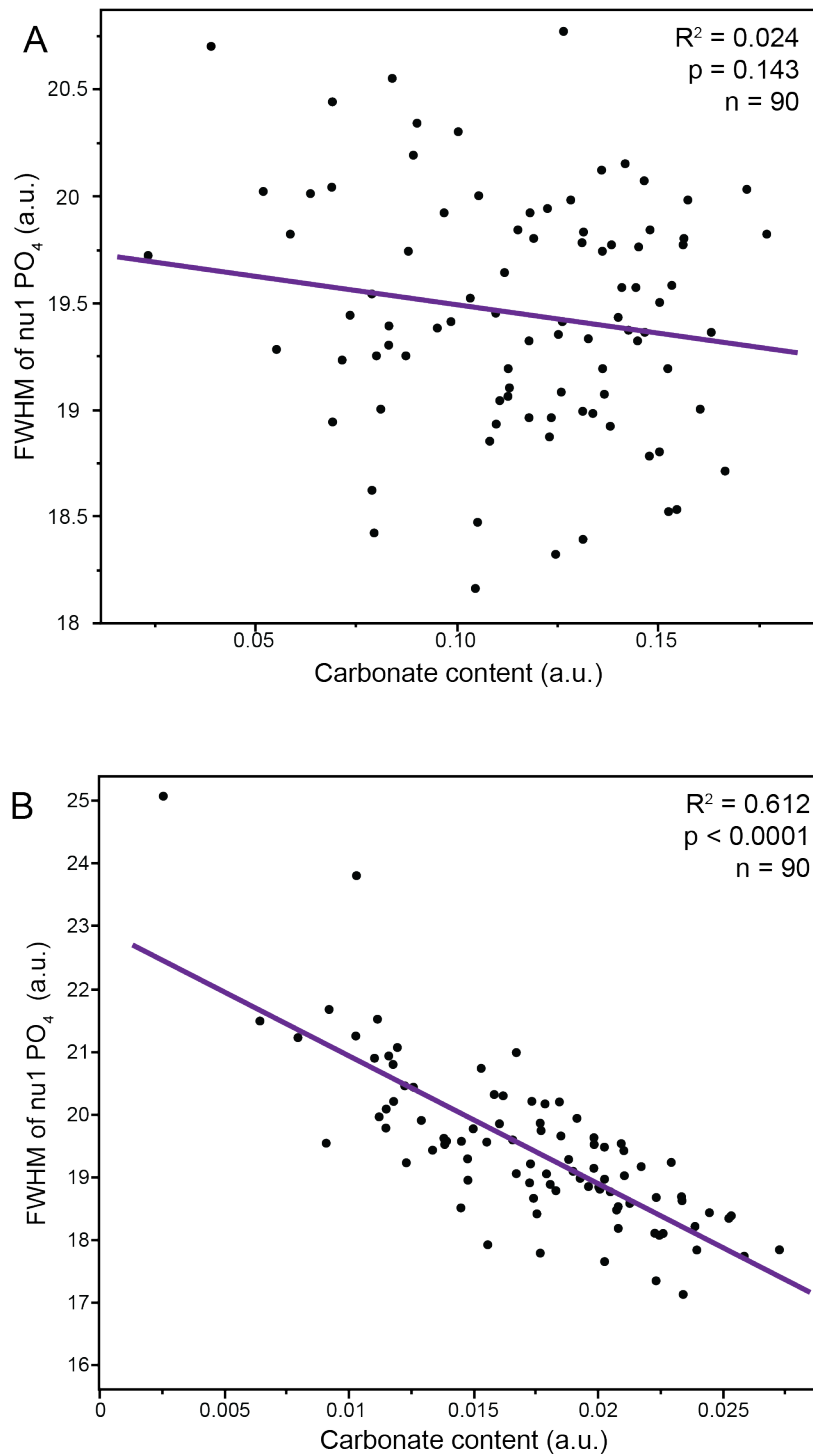


Figure A. 4. Two scatter plots of mineral crystallinity vs. carbonate content. A). Raw data collected from ν_1 PO_4^{3-} and ν_1 CO_3^{2-} are used without any data processing. The Low R^2 and high p-value shows that the two parameters have no relationship. B). Processed data with manual PMMA subtraction and peak fitting (Lorentzian) on ν_1 PO_4^{3-} shows a positive relationship between mineral crystallinity (inverse of

FWHM) and carbonate content. However, since we cannot fully grasp the rationale behind data processing, plot A is chosen for the final configuration.

A.4 Heterogeneity

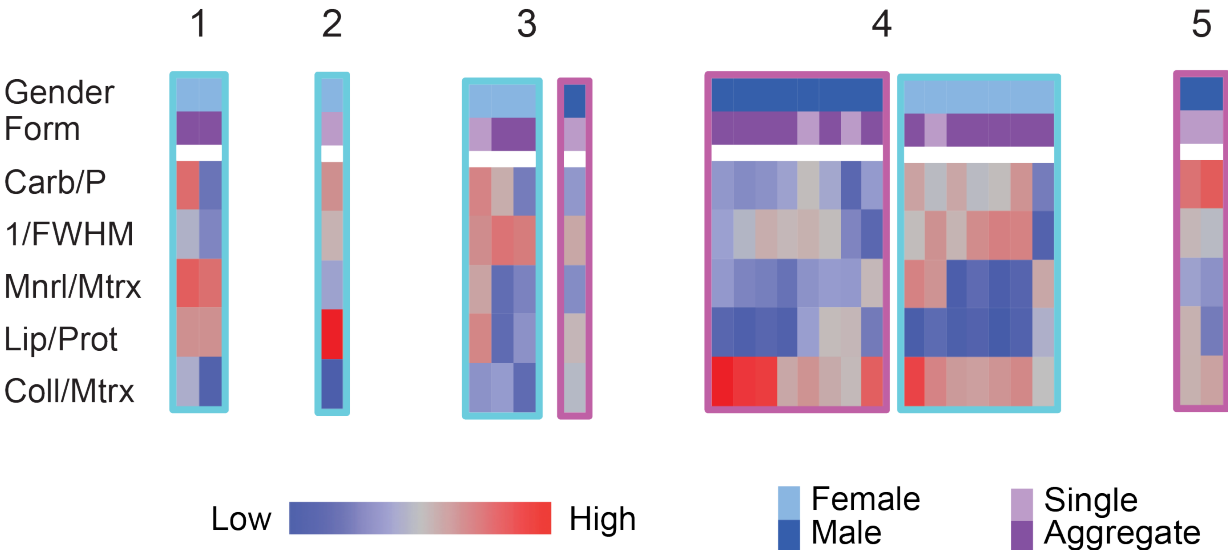


Figure A. 5. Heterogeneity of valvular calcifications across patients. Two types of patients are summarized. Type A patients (cyan, N = 3) have calcifications distributed across 4 out of 5 clusters, while Type B patients (magenta, N = 4) have most calcifications concentrated within one cluster.

Table A. 1. The distribution of 84 calcifications in 5 clusters with respect to patients. Patients with micro-CT scores of 91, 310, and 516 have calcifications dispersed in multiple clusters (type A), while patient with scores of 158, 225, 263, and 434 have calcifications concentrated within a cluster (type B)

Micro-CT #	Cluster 1	Cluster 2	Cluster 3	Cluster 4	Cluster 5	Total
91	2	1	3	7		13
158		1		3	8	12
169			4	1		5
225	1		7	1	1	10
263	1		10	2		13
310		3		2	4	9
434			1	8	2	11
516	2	4		1	4	11
Total	6	9	25	25	19	84

A.5 Raman Peak Assignments

Table A. 2. Raman band assignments. The spectral range of Raman peaks used in this study to calculate peak areas (and peak width).

Vibrational modes	Band assignment (cm ⁻¹)	Notes
ν_1 PO ₄ ³⁻	917.5 – 982.5	For both peak area and FWHM
ν_1 CO ₃ ²⁻	1053 – 1095	
Phe	991 – 1008	Ring breathing mode of phenyl group
Amide III	1216 – 1366	Coupled C-H, N-H deformation modes
Collagen Amide III	1216 – 1284	The first doublet peak of Amide III
NCP Amide III	1295 – 1365	The second peak complex of Made III
CH ₂ twisting	1288 – 1312	Signature of lipid
Symmetric ν (C-H)	2796 – 2860	Key signature of lipid
NCP aromatic	3049 – 3089	
NCP C-H stretch	2908 - 2943	
1600	1590 - 1608	A peak of mystery